Structural dynamic vibration absorber using a tuned inerter eddy current damper

Dawei Li[a], Kohju Ikago[b]*, Ao Yin[b]

[a]School of Civil Engineering, Lanzhou University of Technology, Lanzhou 730050, PR China

[b]International Research Institute of Disaster Science (IRIDeS), Tohoku University, Sendai, 980-8572, Japan

*Corresponding Author: Kohju Ikago; Email: ikago@irides.tohoku.ac.jp

Nomenclature:

Notation	Definition
$\boldsymbol{A}_j$	Magnetic vector potential of the *j*th region
B_r	Residual magnetic flux density of the permanent magnet
$\boldsymbol{B}_j$	Magnetic flux density of the *j*th region
c_s	Damping coefficient of the primary structure
c_e	Equivalent damping coefficient of the IECD
c_0	Critical damping coefficient of the IECD
d_ϕ	Diameter of the ball screw
F_d	Axial force of the IECD
F_e	Eddy current damping force of the IECD
F_f	Friction force of the IECD
F_I	Inertial force of the IECD
$\tilde{F}_\mathrm{f}$	The maximum friction force
$\tilde{F}_\mathrm{fitting}$	The fitted maximum friction value for a rectangle wave with very low frequency
Δ_1	Thickness of the back iron of permanent magnet disk
Δ_2	Thickness of the permanent magnets
Δ_3	Thickness of the air gap between the permanent magnet and conductor
Δ_4	Thickness of the conductor
Δ_5	Thickness of the back iron of conductor disk
$\boldsymbol{H}_j$	Magnetic field intensity in the *j*th region
$\boldsymbol{J}$	Induced current density in region IV
k_s	Stiffness of the primary structure
k_d	Stiffness of the supporting spring
L_d	Lead length of the ball screw
$\boldsymbol{M}$	Magnetization of permanent magnets (region II)
m_s	Mass of the primary structure
m_d	Apparent mass of the IECD
n_p	Number of pole pairs of permanent magnets
P	Power produced by the eddy current effect
r_mg	Radius of circular permanent magnets
R_mg	Location radius of permanent magnets
T_e	Electromagnetic torque of the IECD
v_mg	Tangential velocity of the permanent magnets
v_0	Critical velocity of the IECD
$x_\mathrm{s}, \dot{x}_\mathrm{s}, \ddot{x}_\mathrm{s}$	Acceleration, velocity, and displacement responses of the primary structure
$x_\mathrm{d}, \dot{x}_\mathrm{d}, \ddot{x}_\mathrm{d}$	Acceleration, velocity, and deformation responses of the IECD
$\ddot{x}_0$	Acceleration of the ground motion
$x_\mathrm{s}^\mathrm{max}$	Target inter-story drift of the designed SDOF system
$x_\mathrm{d}^\mathrm{max}$, $\dot{x}_\mathrm{d}^\mathrm{max}$	Target deformation and velocity responses of the IECD in the TIECD system
τ_mg	Edge length of each equivalent rectangular permanent magnets
τ_pole	Pole pitch length of each permanent magnet
σ_c	Conductivity of conductor
ω	Angular velocity of the conductor disk
$\omega_\mathrm{s} = \sqrt{k_\mathrm{s}/m_\mathrm{s}}$	Natural frequency of the undamped primary structure
$\omega_\mathrm{d} = \sqrt{k_\mathrm{d}/m_\mathrm{d}}$	Frequency of the TIECD
$\mu_\mathrm{d} = m_\mathrm{d}/m_\mathrm{s}$	Mass ratio of the TIECD to the primary structure
μ_0	Permeability of free space ($4\pi \times 10^{-7}$ T A/m)
μ_mg	Relative permeability of a permanent magnet
μ_r	Relative permeability of a non-magnetic material
$\gamma_\mathrm{d} = \omega_\mathrm{d}/\omega_\mathrm{s}$	Ratio of the frequency of the TIECD to that of the primary structure
$\zeta_\mathrm{d} = c_\mathrm{e}/2\sqrt{k_\mathrm{s}m_\mathrm{s}}$	Equivalent damping ratio of the TIECD
$\boldsymbol{\phi} = [\phi_\mathrm{s}, \phi_\mathrm{d}]^\mathrm{T}$	Complex eigenvector of the primary structure attached to the equivalent TVMD
κ	Ratio of the threshold velocity $\dot{x}_\mathrm{d}^\mathrm{max}$ to the critical velocity v_0 of the IECD

Abstract

The advantages of eddy current dampers over conventional fluid dampers include the ability to produce resistive forces with no contact between the components, wherein damping forces are generated, resulting in a less degradable mechanism. Thus far, the apparent mass effect, referred to as inertance, in an eddy current damper employing rotational motion has not been intentionally applied for vibration control. Therefore, this paper proposes utilizing the inertance effect in an inerter eddy current damper (IECD) to construct a dynamic vibration absorber for the seismic protection of civil structures, termed as a tuned inerter eddy current damper (TIECD). The IECD consists of a ball screw, a conductor, permanent magnets, and a back iron. The gravitational mass of the back iron disk is converted into inertance via the ball-screw mechanism, which amplifies the mass and damping effects of the rotational disk and eddy currents, respectively, by converting low-speed translational motion into high-speed rotational motion. An analytical method based on the separation of variables is applied to estimate the eddy current damping force of the IECD at different velocities. Concurrently, a succinct damping model is developed to capture the mechanical behavior of the nonlinear eddy current damping. A series of dynamic tests using a small-scale prototype IECD is then conducted to confirm the feasibility and accuracy of the proposed numerical damping model. Next, an equivalent damping coefficient for eddy current damping is derived under harmonic excitation. Based on a combination of the fixed-point method, the equivalent damping coefficient of the IECD, and complex eigenanalysis, an optimal design method for the TIECD is developed. Finally, the effectiveness of the proposed TIECD is validated through a shake table test and a numerical simulation.

Keywords: Eddy current effect; separation of variables; dynamic vibration absorber; tuned inerter eddy current damper (TIECD); optimal design.

1 Introduction

Over the past several decades, the practice of adding supplemental energy dissipators to structures to control their responses to earthquakes and wind loads has become widespread. The development of inerters [1] as vibration control devices has further expanded the possibilities of seismic protective systems for civil structures. In Japan, in 1975, before the term “inerter” was defined, the so-called ball-screw inerter was used as a mechanical snubber to replace a hydraulic snubber for the vibration-proof nuclear power plant piping at the Tokai No. 2 Power Station [2]. Inerters were initially investigated for use in automobile suspension [3] and railroad [4]

applications, before their scope was gradually expanded to include building and civil engineering structures [5–15]. Kawamata proposed a mass pump [16] that could be classified as a fluid inerter [17–19]. Various other types of inerter devices using different mechanisms such as racks and pinions [8,20,21] or electromagnets [22] have also been proposed.

Viscous fluids used in conventional viscous mass dampers are mostly employed to provide damping; however, drawbacks such as the cost of changing the damping coefficient and oil leakage [23] have been identified by researchers. Potential damping mechanics has been developed to address these shortcomings and offer alternatives. Among them, the eddy current effect [24–30] has attracted significant interest among researchers owing to its various benefits, including the absence of mechanical contact friction, stability at high temperatures, and simple form. Furthermore, the intensity of the eddy current effect can be easily adjusted by changing the gap between the magnetic source and conductor [31–34]. Certain devices that use electromotive forces can even serve as energy harvesters [35–38].

The eddy current effect is generated by the relative motion between a non-magnetic conductive material [24,26,28–30] and a magnetic field or by the time-varying intensity of a stationary magnetic field [27,39,40]. Owing to the superiority of the eddy current effect, as mentioned above, it has been broadly implemented in the industry [31,32,41–45], including in vehicle brakes [46–48]. The application of eddy current dampers and eddy-current-based tuned mass dampers to engineering structures has been proposed to exploit their advantages, such as adjustability, stability, and simple topology [49–57]. However, the large apparent mass effect (inertance) resulting from the small physical mass in a rotary eddy current damper has not been exploited thus far. Therefore, this work proposes using the inertance generated by a rotary eddy current damper to construct an efficient structural dynamic vibration absorber without a weight penalty. Alternatively, attempts to develop a hybrid strategy that incorporates the eddy current effect with the use of shape memory alloys [58], magnetorheological fluids [59], and friction [60,61] have been undertaken to improve damper control performance. It should be noted that traditional eddy current damping employs the translational motion of the magnetic source and conductor, leading to a low damping density, as compared with the cost and size of the damper [49,50,57]. In addition to replacing the conductor material with a higher conductivity and reducing the air gap between permanent magnets and conductors [33], magnification of the relative velocity between the permanent magnets and conductors represents a more effective approach. Indeed, using ball screw mechanics [62–64] or a rack–gear system [65–67] can magnify the relative velocity between the two terminals by up to 10 times, resulting in considerable amplification of the damping.

In addition to the development of new techniques to enhance the energy dissipation of inerter-based dampers, challenges have been identified in developing effective inerter system

configurations and determining the appropriate design parameters. Tuned viscous mass dampers (TVMDs) [5,6,14], tuned inerter dampers (TIDs) [9,15,68], and tuned mass damper inerters (TMDIs) [12,18,69–71] have been developed by altering the topology of the inerter, damper, and spring. Owing to its cost-effective amplification of energy dissipation, the TVMD has attracted considerable attention for its control mechanism and the development of optimal design methods [5,6,72,73]. In the proposed tuned inerter eddy current damper (TIECD), the inertance and damping amplification effects of a rotating eddy current damper [34,62] are fully utilized as a component of a TVMD to construct a compact dynamic vibration absorber without a weight penalty [5,72]. Unlike previous studies on eddy current damping devices without tuning springs [62,67,74,75], the proposed TIECD offers excellent energy dissipation capacity based on the damping enhancement principle [5,72], with the optimal combination of a tuning spring and the IECD.

Herein, we present a systematic investigation of the proposed TIECD. We provide the results of theoretical analyses and the experimental validation of the IECD, describe an optimal design with an equivalent damping model, and present the results of a shake table test for the TIECD. The electromagnetic field in moving eddy current problems can be solved using the magnetic equivalent circuit (MEC) model [76,77], field analysis method [31,32,43,46,62], and finite element method [34,67]. The finite element method can deal with complex configurations and offer precise results, albeit at the expense of the computational time. Accurate simulation results for the MEC model are strongly dependent on the known flux path and the moderate eddy current effect. In comparison with the two aforementioned methods, the field analytical method with a clear physical meaning and fewer computational resources was adopted in this study to approximate the electromagnetic torque of the inerter eddy current damper (IECD) [31,32,78]. To investigate the influence of the skin effect of the conductor and the nonlinearity in the permeability of the back iron on eddy current damping [32], a finite element analysis considering the saturation of the back iron [32,48] was conducted using the finite element method magnetics (FEMM) software [79]. A succinct equation for eddy current damping was then fitted to represent the mechanical behavior of the eddy current damping force according to the input velocity over a significantly large range [25,30,63]. In addition, a series of dynamic tests was conducted for the IECD under harmonic excitation at various frequencies, and the influence of the air gap between the permanent magnets and conductor on the eddy current damping was investigated. Furthermore, an equivalent relationship between the eddy current damping and linear viscous damping was derived to associate the behavior of the IECD with that of a viscous mass damper (VMD). Subsequently, an optimal design procedure for the TIECD was established by combining the complex eigenanalysis, fixed-point method, and equivalent damping model. Numerical simulations and shake table tests for a single-degree-of-

freedom (SDOF) system were also conducted by employing natural ground motions, to verify the seismic control effect of the designed TIECD.

The remainder of this paper is organized as follows. Section 2 presents the outline of the developed IECD. Section 3 describes the analytical formulation of the eddy current damping force employed in the proposed IECD. Detailed information related to the realization of a small-scale IECD and the performance test observations are provided in Section 4, in addition to the derivation of an equivalent damping coefficient for the eddy current damping. In Section 5, the novel TIECD is described, its optimal design method is explained, and the results of the shake table test to verify its control effect are presented. Lastly, conclusions and remarks are presented in Section 6.

2 Outline of inerter eddy current damper

As illustrated in Fig. 1, a rotary IECD comprises a screw shaft, a ball nut, a back iron, a conductor, and permanent magnets. Considerable inertial resistive and damping forces are generated by the mass moment inertia of the rotary disk and the electromagnetic damping forces induced by the relative circumferential motion between the conductor and permanent magnets. Therefore, the total axial resistive force F_{d} of the ball screw is expressed as the sum of the inertial force F_{I}, eddy current damping force F_{e}, and mechanical friction force F_{f}, as follows:

$$F_{\mathrm{d}} = F_{\mathrm{I}} + F_{\mathrm{e}} + F_{\mathrm{f}}. \tag{1}$$

The inertial force F_{I} is expressed as

$$F_{\mathrm{I}} = m_{\mathrm{d}}\ddot{x}_{\mathrm{d}}, \tag{2}$$

where $\ddot{x}_{\mathrm{d}}$ is the relative acceleration response of the two terminals in the IECD; $m_{\mathrm{d}} = J_{\mathrm{t}}a_{\mathrm{d}}$ denotes the inertance, in which J_{t} is the mass moment of inertia of the disk, $a_{\mathrm{d}} = (2\pi/L_{\mathrm{d}})^2$, and L_{d} is the lead length of the ball screw.

The eddy current damping force F_{e} is given by

$$F_{\mathrm{e}} = \left(\frac{2\pi}{L_{\mathrm{d}}}\right) T_{\mathrm{e}}(\dot{x}_{\mathrm{d}}), \tag{3}$$

where $\dot{x}_{\mathrm{d}}$ and $T_{\mathrm{e}}(\dot{x}_{\mathrm{d}})$ denote the relative velocity responses of the two terminals in the IECD and electromagnetic torque induced by the eddy current effect, respectively. A detailed approximation method for T_{e} is presented in Section 3.

Mechanical friction exists at the contact surface between the ball bearings and screw threads [80]. Because the ball bearings are preloaded, their frictional force is negligibly affected by the external force acting on the ball screw or the velocity in the axial direction. The Coulomb friction model [81] with a smaller friction coefficient was adopted to approximate the rolling contact friction, in order to express the friction force F_{f}:

$$F_{\mathrm{f}} = \tilde{F}_{\mathrm{f}}\mathrm{sgn}(\dot{x}_{\mathrm{d}}), \tag{4}$$

where $\tilde{F}_{\mathrm{f}}$ denotes the maximum friction force identified using a very low frequency test, and $\mathrm{sgn}(\cdot)$ denotes the signum function.

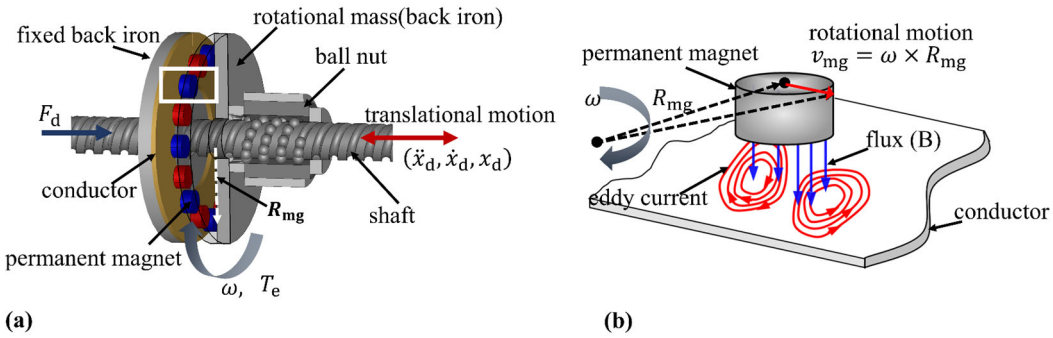

Fig. 1 (a) Schematic of IECD and (b) eddy current effect in electromagnetic field.

3 Determination of electromagnetic torque

As mentioned in Section 2, the electromagnetic torque of the IECD is generated by the relative motion between the conductor and permanent magnets in the circumferential direction. According to the electromagnetic field theory [82], Maxwell's equations can describe this electromagnetic behavior in an IECD. Owing to the small ratio of the permanent magnet radius r_{mg} to its distance from the central location R_{mg}, the velocity of the permanent magnets at its center, $v_{\mathrm{mg}} = \omega R_{\mathrm{mg}}$, can be used to calculate the eddy current damping forces. Using the general equivalence principle proposed by Wang et al. [32], permanent magnet shapes were transformed into rectangles with the same area. The original 3-D model can then be transformed into a 2-D analytical model in the Cartesian coordinate system, as shown in Fig. 2.

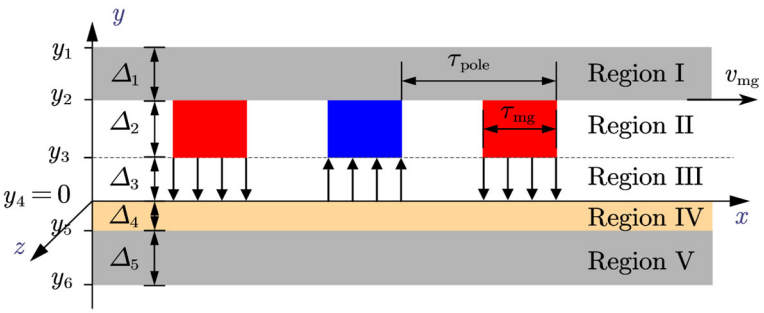

Fig. 2 Analytical model of electromagnetic field.

In Fig. 2, τ_{mg} and $\tau_{\mathrm{pole}} = \pi R_{\mathrm{mg}}/n_{\mathrm{p}}$ denote the edge and pole pitch lengths of the equivalent permanent magnets, respectively, where n_{p} denotes the number of permanent magnet pole pairs. As shown in Fig. 2, the electromagnetic field in the IECD is composed of five regions: (I) the back iron of the magnetic disk, (II) permanent magnets and intermediate air, (III) air gap, (IV) conductor, and (V) back iron of the conductor. As documented in [83], the curvature ratio defined by the radial edge length of the equivalent magnets to the pole pitch length τ_{pole} is not greater than unity, and the influence of the curvature effect is less than 5%, which can be

neglected in this calculation. Additionally, three assumptions are adopted: 1) the relative permeability and conductivity of the permanent magnets are $\mu_{\mathrm{mg}} = 1$ and $\sigma_{\mathrm{mg}} = 0$, respectively, and the relative conductivity of the air is $\sigma_{\mathrm{a}} = 0$; 2) the thickness of the back iron is sufficient to avoid magnetic saturation, and its relative permeability is constant; 3) the conductor in region IV and back iron in region V remain stationary, and the permanent magnets in region II and back iron in region I move with velocity v_{mg}.

Considering $\boldsymbol{A} = [0; 0; A_z(x, y)]$ as a magnetic vector potential, the flux density $\boldsymbol{B} = \left[B_x(x, y), B_y(x, y), 0\right]$ can be expressed as

$$\boldsymbol{B} = \nabla \times \boldsymbol{A}. \tag{5}$$

Using the Coulomb gauge condition $\nabla \cdot \boldsymbol{A} = 0$ [82], the following equation holds:

$$\nabla \times \nabla \times \boldsymbol{A} = \nabla \cdot (\nabla \cdot \boldsymbol{A}) - \nabla^2 \boldsymbol{A} = -\nabla^2 \boldsymbol{A} = \nabla \times \boldsymbol{B}. \tag{6}$$

The constitutive relation of the electromagnetic field can then be given as

$$\boldsymbol{B} = \mu_0\left(\mu_{\mathrm{r}}\boldsymbol{H} + \mu_{\mathrm{mg}}\boldsymbol{M}\right), \tag{7}$$

where μ_{r} and μ_{mg} are the relative permeabilities of the non-magnetic material and permanent magnets, respectively; $\boldsymbol{H} = \left[H_x(x, y), H_y(x, y), 0\right]$ is the magnetic field intensity; and $\boldsymbol{M} = \left[0; M_y(x, y); 0\right]$ is the magnetization of the permanent magnet. According to Ampere's law,

$$\nabla \times \boldsymbol{H} = \boldsymbol{J}, \tag{8}$$

where $\boldsymbol{J} = [0; 0; J_{\mathrm{z}}(x, y)]$ is the induced current density, expressed as the product of the electrical conductivity of the material and the electric field intensity, that is, $\boldsymbol{J} = \sigma\boldsymbol{E}$. Thus, according to Farah's law,

$$\nabla \times \boldsymbol{E} = -\partial\boldsymbol{B}/\partial t, \tag{9}$$

Substituting Eqs. (7)–(9) into Eq. (6), the governing equation for the electromagnetic field in the IECD can be obtained as follows:

$$\nabla^2 \boldsymbol{A} = \mu_0\left(\mu_{\mathrm{r}}\sigma\frac{\partial \boldsymbol{A}}{\partial t} - \mu_{\mathrm{mg}}\nabla \times \boldsymbol{M}\right). \tag{10}$$

3.1 Governing equations for regions I and III

As there is no relative motion between the permanent magnets and the related back iron, the magnetic vector potential remains constant in region I. Therefore, the governing equation for region I is expressed as

$$\frac{\partial^2 A_z^{\mathrm{I}}}{\partial x^2} + \frac{\partial^2 A_z^{\mathrm{I}}}{\partial y^2} = 0, \tag{11}$$

where A_z^{I} is the modulus of the magnetic vector potential in region I.

The insulating property of air implies that the governing equation for region III is similar to that for region I; thus,

$$\frac{\partial^2 A_z^{\mathrm{III}}}{\partial x^2}+\frac{\partial^2 A_z^{\mathrm{III}}}{\partial y^2}=0, \tag{12}$$

where A_z^{III} is the modulus of the magnetic vector potential in region III.

3.2 Governing equation for region II

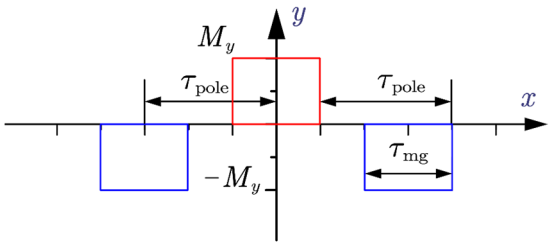

Fig. 3 Definition of harmonic magnetization along with *x*-axis.

As illustrated in Fig. 3, the magnetization distribution of the permanent magnets $M_y(x,y)$ can be modeled as a rectangular wave along the *x*-axis [31,32]. Thus, the Fourier series $\widetilde{M}_y(x,y)$ is used to approximate $M_y(x,y)$, as follows:

$$\widetilde{M}_y(x,y)=\sum_{n=1,3,5,\ldots}^{N} M_{y,n}\exp(-i\beta x), \tag{13}$$

$$M_{y,n}=\frac{1}{\tau_{\mathrm{pole}}}\int_{-\tau_{\mathrm{pole}}}^{\tau_{\mathrm{pole}}} M_y\cos\frac{n\pi}{\tau_{\mathrm{pole}}}x\mathrm{d}x=\frac{4M_y}{n\pi}\sin\frac{n\pi\tau_{\mathrm{mg}}}{2\tau_{\mathrm{pole}}}, \tag{14}$$

where $\beta=n\pi/\tau_{\mathrm{pole}}$, $i=\sqrt{-1}$, $\exp(\cdot)$ is the exponential function, $M_y=B_r/\left(\mu_{\mathrm{mg}}\mu_0\right)$, B_{r} is the residual flux density, and μ_{mg} denotes the relative permeability of the permanent magnets. Substituting the assumptions that $\mu_{\mathrm{mg}}=1$ and $\sigma_{\mathrm{mg}}=0$ into Eq. (10), the governing equation for region II with the first-order component of the Fourier series is given by

$$\frac{\partial^2 A_z^{\mathrm{II}}}{\partial x^2}+\frac{\partial^2 A_z^{\mathrm{II}}}{\partial y^2}=i\mu_{\mathrm{mg}}\mu_0\beta M_{y,1}\exp(-i\beta x), \tag{15}$$

where A_z^{II} is the modulus of the magnetic vector potential in region II.

3.3 Governing equations for regions IV and V

In regions IV and V, the currents induced in the conductor and back iron were generated by the time-dependent variations in the electromagnetic field intensity. Therefore, the governing equations for regions IV and V can be derived from Eqs. (10), as follows:

$$\frac{\partial^2 A_z^{\mathrm{IV}}}{\partial x^2}+\frac{\partial^2 A_z^{\mathrm{IV}}}{\partial y^2}=\mu_0\mu_{\mathrm{r}}^{\mathrm{IV}}\sigma^{\mathrm{IV}}\frac{\partial A_z^{\mathrm{IV}}}{\partial t}, \tag{16}$$

$$\frac{\partial^2 A_z^{\mathrm{V}}}{\partial x^2}+\frac{\partial^2 A_z^{\mathrm{V}}}{\partial y^2}=\mu_0\mu_{\mathrm{r}}^{\mathrm{V}}\sigma^{\mathrm{V}}\frac{\partial A_z^{\mathrm{V}}}{\partial t}, \tag{17}$$

where $\mu_{\mathrm{r}}^{\mathrm{IV}}$ and $\mu_{\mathrm{r}}^{\mathrm{V}}$ denote the relative permeabilities, and σ^{IV} and σ^{V}denote the electrical conductivities of the conductor with the related back iron in regions IV and V, respectively.

3.4 Solution of governing equations

Using the separation of variables method (SVM), a general solution of the governing equations for the five regions can be defined as the product of two independent components:

$$A_z^j(x,y) = A_{z,y}^j(y)\exp(-i\beta x), j = \mathrm{I}, \mathrm{II}, \mathrm{III}, \mathrm{IV}, \mathrm{V}. \quad (18)$$

The solutions of the magnetic vector potential can then be constructed for the five regions, as follows:

$$\begin{aligned}
A_z^{\mathrm{I}}(x,y) &= \left(C^{\mathrm{I}}\exp(\beta y) + D^{\mathrm{I}}\exp(-\beta y)\right)\exp(-i\beta x)\\
A_z^{\mathrm{II}}(x,y) &= \left(C^{\mathrm{II}}\exp(\beta y) + D^{\mathrm{II}}\exp(-\beta y)\right)\exp(-i\beta x) - \frac{i}{\beta}\mu_0 M_{y,1}(x)\exp(-i\beta x)\\
A_z^{\mathrm{III}}(x,y) &= \left(C^{\mathrm{III}}\exp(\beta y) + D^{\mathrm{III}}\exp(-\beta y)\right)\exp(-i\beta x)\\
A_z^{\mathrm{IV}}(x,y) &= \left(C^{\mathrm{IV}}\exp\left(\beta^{\mathrm{IV}} y\right) + D^{\mathrm{IV}}\exp\left(-\beta^{\mathrm{IV}} y\right)\right)\exp(-i\beta x)\\
A_z^{\mathrm{V}}(x,y) &= \left(C^{\mathrm{V}}\exp\left(\beta^{\mathrm{V}} y\right) + D^{\mathrm{I}}\exp\left(-\beta^{\mathrm{V}} y\right)\right)\exp(-i\beta x),
\end{aligned} \quad (19)$$

where $\beta^{\mathrm{IV}} = \sqrt{\beta^2 - i\beta\mu_{\mathrm{r}}^{\mathrm{IV}}\mu_0\sigma^{\mathrm{IV}}v_{\mathrm{mg}}}$, $\beta^{\mathrm{V}} = \sqrt{\beta^2 - i\beta\mu_{\mathrm{r}}^{\mathrm{V}}\mu_0\sigma^{\mathrm{V}}v_{\mathrm{mg}}}$, and $v_{\mathrm{mg}} = \omega R_{\mathrm{mg}}$.

The boundary conditions (BCs) at y_1 and y_6 and the continuous conditions (CCs) at the interfaces of two adjacent regions are given as follows:

$$\begin{aligned}
&\mathrm{BC(I)}: \frac{\partial A_z^{\mathrm{I}}}{\partial x} = 0|_{y=y_1}\\
&\mathrm{CC(I–II)}: \frac{\partial A_z^{\mathrm{I}}}{\partial x} = \frac{\partial A_z^{\mathrm{II}}}{\partial x}|_{y=y_2} \qquad \frac{1}{\mu_{\mathrm{s}}}\frac{\partial A_z^{\mathrm{I}}}{\partial y} = \frac{1}{\mu_0}\frac{\partial A_z^{\mathrm{II}}}{\partial y}|_{y=y_2}\\
&\mathrm{CC(II–III)}: \frac{\partial A_z^{\mathrm{II}}}{\partial x} = \frac{\partial A_z^{\mathrm{III}}}{\partial x}|_{y=y_3} \qquad \frac{1}{\mu_0}\frac{\partial A_z^{\mathrm{II}}}{\partial y} = \frac{1}{\mu_0}\frac{\partial A_z^{\mathrm{III}}}{\partial y}|_{y=y_3}\\
&\mathrm{CC(III–IV)}: \frac{\partial A_z^{\mathrm{III}}}{\partial x} = \frac{\partial A_z^{\mathrm{IV}}}{\partial x}|_{y=y_4=0} \qquad \frac{\partial A_z^{\mathrm{III}}}{\partial y} = \frac{1}{\mu_{\mathrm{r}}^{\mathrm{IV}}}\frac{\partial A_z^{\mathrm{IV}}}{\partial y}|_{y=y_4=0}\\
&\mathrm{CC(IV–V)}: \frac{\partial A_z^{\mathrm{IV}}}{\partial x} = \frac{\partial A_z^{\mathrm{V}}}{\partial x}|_{y=y_5} \qquad \frac{1}{\mu_{\mathrm{r}}^{\mathrm{IV}}}\frac{\partial A_z^{\mathrm{IV}}}{\partial y} = \frac{1}{\mu_{\mathrm{r}}^{\mathrm{V}}}\frac{\partial A_z^{\mathrm{V}}}{\partial y}|_{y=y_5}\\
&\mathrm{BC(V)}: \frac{\partial A_z^{\mathrm{V}}}{\partial x} = 0|_{y=y_6}
\end{aligned} \quad . (20)$$

Substituting Eq. (19) into Eq. (20), the coefficients related to the solutions for the five regions can be estimated via symbolic calculations. The symbolic computational tools provided in Sagemath [84], an open-source software, were employed to derive the closed-form solution. The flux density in region IV was estimated as follows:

$$B_y^{\mathrm{IV}} = \frac{\partial A_z^{\mathrm{IV}}}{\partial x} = -i\beta\left(C^{\mathrm{IV}}\exp\left(\beta^{\mathrm{IV}} y\right) + D^{\mathrm{IV}}\exp\left(-\beta^{\mathrm{IV}} y\right)\right)\exp(-i\beta x). \quad (21)$$

Furthermore, the induced current density in region IV was determined as

$$J_z^{\mathrm{IV}} = -\sigma^{\mathrm{IV}}\frac{\partial A_z^{\mathrm{IV}}}{\partial x} = -i\sigma^{\mathrm{IV}}\omega R_{\mathrm{mg}}\beta\left(C^{\mathrm{IV}}\exp\left(\beta^{\mathrm{IV}} y\right) + D^{\mathrm{IV}}\exp\left(-\beta^{\mathrm{IV}} y\right)\right)\exp(-i\beta x). \quad (22)$$

Although the back iron in region V generates eddy currents, its contribution can be ignored owing to the rapid decay of the flux density with an increase in the distance from the surface of the permanent magnet and the low conductivity of the material [46]. Therefore, the total

electromagnetic torque generated by n_{p} pairs of magnets can be expressed as

$$\begin{aligned} T_{\mathrm{e}}^{0} &= \frac{P}{\omega} = \frac{n_{\mathrm{p}}}{2\omega\sigma^{\mathrm{IV}}} \int_{\mathrm{volume}} \{J_z^{\mathrm{IV}}\}^* J_z^{\mathrm{IV}} \mathrm{d}V \\ &= \frac{n_{\mathrm{p}}\sigma^{\mathrm{IV}}\omega\beta^2 R_{\mathrm{mg}}^2 w_{\mathrm{mg}}\tau_{\mathrm{pole}}}{2} \int_{-\Delta_4}^{0} \left| C^{\mathrm{IV}}\exp\left(\beta^{\mathrm{IV}} y\right) + D^{\mathrm{IV}}\exp\left(-\beta^{\mathrm{IV}} y\right)\right|^2 \mathrm{d}y, \end{aligned} \tag{23}$$

where w_{mg} is the width of the equivalent permanent magnet. To consider the distribution and actual path of the induced current in the overhang region [32,47,76,77], the modification factor k_{Russel} [78] is used to obtain the electromagnetic torque in the 3-D analytical model; correcting the torque in the 2-D analytical results yields the following:

$$T_{\mathrm{e}} = k_{\mathrm{Russel}} T_{\mathrm{e}}^{0}, \tag{24}$$

where

$$k_{\mathrm{Russel}} = 1 - \frac{\tanh\lambda_{\mathrm{m}}}{\lambda_{\mathrm{m}}(1+\tanh\lambda_{\mathrm{m}}\tanh\lambda_{\mathrm{cm}})}. \tag{25}$$

Here, $\lambda_{\mathrm{m}} = \pi\tau_{\mathrm{mg}}/(2\tau_{\mathrm{pole}})$, $\lambda_{\mathrm{cm}} = \pi(w_{\mathrm{c}} - w_{\mathrm{mg}})/(2\tau_{\mathrm{pole}})$, and w_{c} is the width of the conductor. It is worth noting that Eq. (25) holds for a variable velocity between the permanent magnets and conductor in the IECD, because the eddy current induced by a moving electromagnetic source in a stationary conductor is equivalent to that induced by a time-dependent electromagnetic field intensity in a stationary conductor [78].

4 Performance tests for IECD

In this section, the dynamic test conducted using a small-scale IECD is discussed to verify the proposed mechanical model of the IECD and the effectiveness of the eddy current damping.

4.1 Outline of IECD

A small-scale IECD was designed, as shown in Fig. 4 (a). A set of ball screws and ball nuts with lead length $L_{\mathrm{d}} = 32$ mm and nominal diameter $d_{\phi} = 32$ mm was employed to transfer the translational motion between the terminals into the rotational motions of the permanent magnets and back iron. As illustrated in Fig. 4 (a), the inertance (apparent mass) of the IECD was $m_{\mathrm{d}} = 451$ kg, provided by a rotational mass consisting of the back iron (371 kg), permanent magnets (17 kg), and an aluminum template serving as a positioning guide for the magnets (63 kg). The back iron was manufactured using SS400 steel, and its permeability ratio (relative to that of air) was assumed to be 1000. It was 12 mm thick and sufficient to avoid magnetic saturation. Copper with high electrical conductivity was selected as the conductive material. Given a ball screw lead length of $L_{\mathrm{d}} = 32$ mm, the air gap was designed to be $\Delta_3^1 = 10$ mm to realize the optimal combination of the inertance and eddy current damping coefficient in the TIECD. The other design parameters related to the eddy current damping force are listed in Table 1.

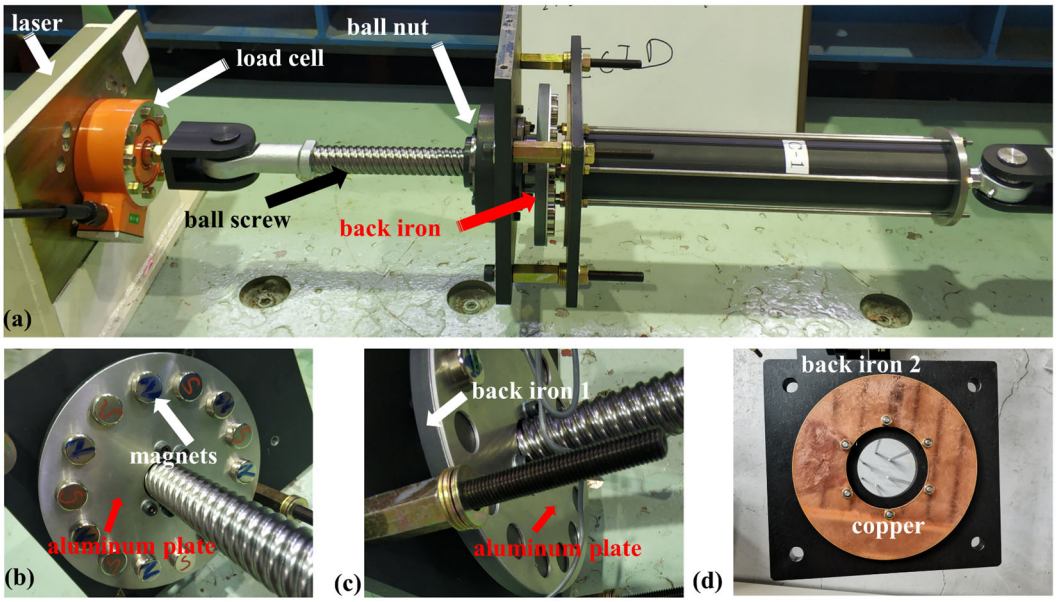

Fig. 4 (a) Arrangement of the IECD test, (b) permanent magnets, (c) back iron and aluminum fixture of magnets, and (d) conductor.

Table 1 Design parameters related to eddy current damping force.

Parameters	Value [Unit]
B_r	1.2 [T]
σ_c^{copper}	59.6 [MS/m]
σ_c^{steel}	6.99 [MS/m]
μ_r^{copper}	1
μ_r^{steel}	1000
n_p	7
r_{mg}	10 [mm]
R_{mg}	70 [mm]
w_c	40 [mm]
Δ_1	12 [mm]
Δ_2	10 [mm]
Δ_3^1	10 [mm]
Δ_3^2	5 [mm]
Δ_4	4 [mm]
Δ_5	12 [mm]

4.2 Approximation of the designed damping force

Assuming that the equivalent shape of the permanent magnets was a square, the length of each edge was $w_{mg} = \tau_{mg} = 17.7$ mm. The pole pitch length of the permanent magnets was estimated as $\tau_{pole} = \pi R_{mg}/n_p = 31.4$ mm. A reasonable copper width in the z-direction w_c should be less than twice the equivalent width of the permanent magnets. As listed in Table 1, the width of copper, $w_c = 40$ mm, was more than twice the equivalent width of the permanent magnets; therefore, the width of the conductor was selected as $2w_{mg} = 35$ mm. Given that the translational relative velocity between the terminals varies from 0 to 0.7 m/s, the circumferential velocity of the permanent magnets increases from 0 to 9.62 m/s. The air gap of the IECD was

set as $\Delta_3^1 = 10$ mm and $\Delta_3^2 = 5$ mm to investigate its influence on the eddy current damping force. The estimated eddy current damping forces obtained using the methods provided in Sections 2 and 3 are represented by the blue circles in Figs. 5 (a) and 5 (b), respectively.

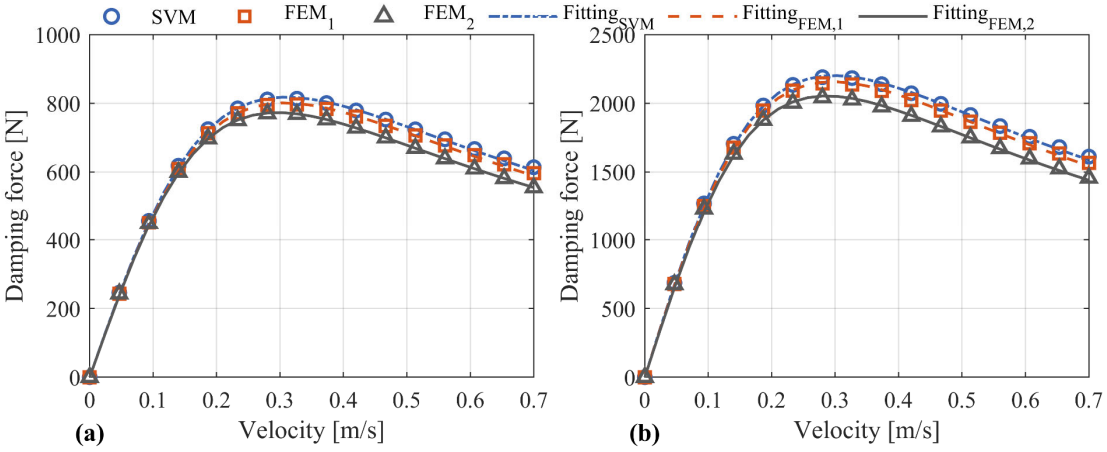

Fig. 5 Comparison of damping forces for (a) $\Delta_3^1 = 10$ mm and (b) $\Delta_3^2 = 5$ mm.

The finite element method was applied to solve the electromagnetic field equations, as discussed in Section 3, to validate the accuracy of the SVM and explore the influences of the skin effect [85] on the conductor and magnetic saturation of the back iron in region V. The 2-D open-source FEMM software [79] developed by Dr. David Meeker was employed to simulate the electromagnetic field, as shown in Fig. 2. According to the equivalent current model in [82], the constant rotational velocity of the permanent magnet was modeled as an electromagnet subjected to an alternating current with a designated frequency in FEMM. As in the case of the SVM, the computed results in FEMM are corrected with the modification factor k_{Russel} to account for the distribution and actual path of the induced current in the overhang region. The simulated results using FEMM based on the assumption of a linear back iron should be equal to the results obtained from the SVM. To investigate the influence of the nonlinear back iron, finite element analyses were also conducted using FEMM with the nonlinear B–H relationship, as shown in Fig. 6. The simulated results based on the linear and nonlinear assumptions were designated as FEM_1 and FEM_2, respectively, as shown in Fig. 5.

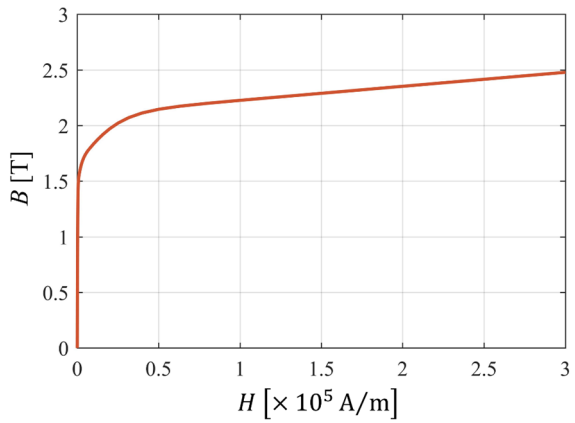

Fig. 6 Nonlinear B–H relationship of back iron.

Figure 5 shows that the simulated SVM results nearly overlap the finite element simulation results FEM_1 based on the linear assumption, when the input velocity is no greater than the critical velocity corresponding to the peak eddy current damping force. As the input velocity exceeds the critical velocity, the divergence between the SVM and FEM_1 progressively increases. This is attributed to the aggravation of the skin effect induced by the eddy current with an increase in the input velocity [85]. As illustrated in Figs. 5 (a) and 5 (b), the simulation results FEM_2 coincide with FEM_1 when the input velocity is less than $0.2\ \mathrm{m/s}$. The growing discrepancies between them are attributed to the nonlinear permeability and even saturation of the back iron in region V. On comparing Figs. 5 (a) and 5(b), the damping force can be observed to increase by a factor of three as the air gap decreases from 10 mm to 5 mm, with peak damping forces of 818 N and 2201 N, respectively, under the linear assumption, and 773 N and 2050 N, respectively, under the nonlinear assumption. The discrepancies between the estimated results of the SVM and nonlinear FEM were 5.5% and 6.9% for the air gaps of 10 mm and 5 mm, respectively. These small errors indicate that the proposed SVM method can be confidently used to approximate the eddy current damping force in the preliminary design of the IECD.

Although an analytical formulation of the equivalent damping force can be derived, exhaustive expressions for the coefficients related to the electromagnetic field equation may hinder their practical application. To describe the mechanical behavior of the eddy current damping force more concisely, the fitting model proposed by Wouterse [25] and Tonoli [30] can be applied, as follows:

$$F_{\mathrm{e}} = c_0 \frac{v_0^2}{\dot{x}_{\mathrm{d}}^2 + v_0^2} \dot{x}_{\mathrm{d}}, \tag{26}$$

where the coefficients describing the critical damping c_0 and critical velocity v_0 remain constant and are obtained from the computational results, as shown in Fig. 5. The fitting parameters of the eddy current damping are summarized in Table 2. Figure 5 shows that the derived fitting model using the parameters listed in Table 2 perfectly captures the mechanical characteristics of the eddy current damping, regardless of the linearity assumption applied. Thus far, SVM-based simulation results have been used to approximate the eddy current damping force in the preliminary design of the IECD. Thus, based on Sections 3 and 4.1, by substituting Eq. (26) into Eq. (1), the total axial force can be expressed as

$$F_{\mathrm{d}} = m_{\mathrm{d}} \ddot{x}_{\mathrm{d}} + c_0 \frac{v_0^2}{\dot{x}_{\mathrm{d}}^2 + v_0^2} \dot{x}_{\mathrm{d}} + \tilde{F}_{\mathrm{f}} \mathrm{sgn}(\dot{x}_{\mathrm{d}}). \tag{27}$$

To validate the accuracy of the proposed damping model and determine the values of the parameters collected in the mechanical model of the IECD, a dynamic test was conducted on the designed IECD under harmonic excitations with various frequencies.

Table 2 Fitting parameters related to the eddy current damping model.

Δ_3	Parameters	SVM	FEM_1	FEM_2
10 mm	c_0	5286	5219	5218
	v_0	0.309	0.307	0.296
5 mm	c_0	14763	14597	14322
	v_0	0.298	0.295	0.287

4.3 Dynamic test on IECD with harmonic inputs

In the dynamic test, the amplitude of the harmonic excitation was set to 30 mm, and sinusoidal excitation with a very low frequency of 0.05 Hz was employed to identify the maximum friction force $\tilde{F}_f$ of the pre-loading ball nut in the designed IECD [80,81], as illustrated in Fig. 7.

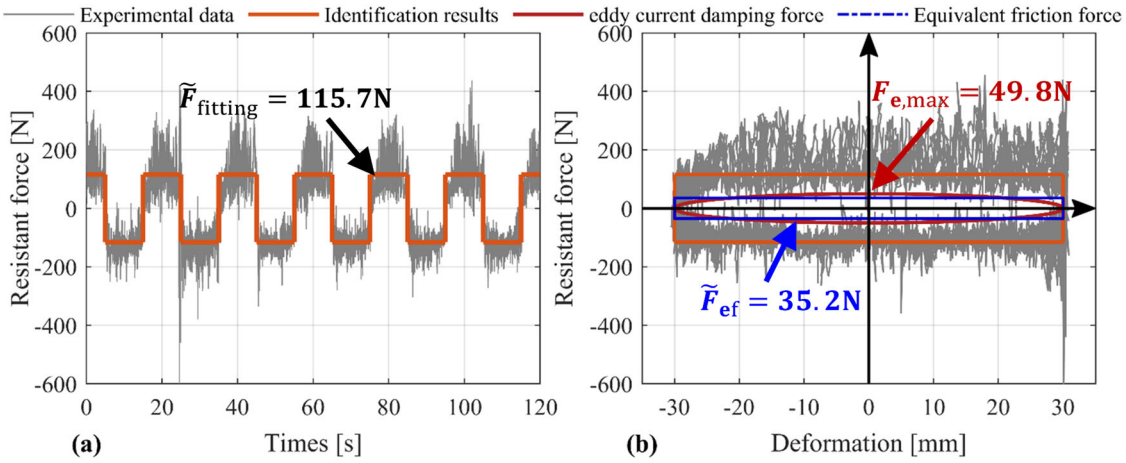

Fig. 7 (a) Time history and (b) hysteretic loop of the resistance force under sinusoidal excitation of 0.05 Hz (amplitude = 30 mm, $\Delta_3^1 = 10$ mm, and sampling rate = 100 Hz).

As shown in Fig. 7 (a), the fitting value for a rectangular wave that includes the contributions from friction and eddy current damping was identified as $\tilde{F}_{\text{fitting}} = 115.7$ N. However, the red line in Fig. 7 (b) suggests that the eddy current force with the maximum value $F_{e,\max} = 49.8$ N needs to be eliminated. To remove the influence of the eddy current damping force, an equivalent force $\tilde{F}_{ef}$ with a rectangular shape was defined using the equivalent energy dissipation of the eddy current damping force F_e. As indicated in Fig.7 (b), the value of $\tilde{F}_{ef}$ was identified as 35.2 N. Therefore, a corrected approximation of the friction force was obtained with the maximum amplitude $\tilde{F}_f = 115.7 - 35.2 \approx 81$ N in a direction opposite to that of the velocity.

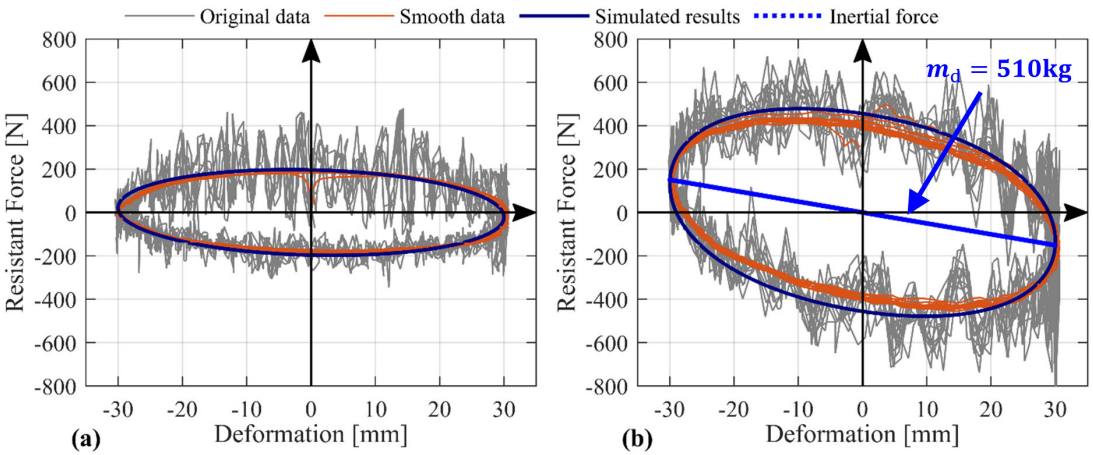

Fig. 8 Hysteretic loop of IECD under sinusoidal excitations of (a) 0.2 Hz and (b) 0.5 Hz (amplitude = 30 mm, $\Delta_3^1 = 10$ mm, and sampling rate = 100 Hz).

The hysteretic loops of the designed IECD under sinusoidal excitations of 0.2 Hz and 0.5 Hz are compared in Fig. 8. This figure shows that the proposed model provides excellent approximations of the hysteretic behaviors under both sinusoidal excitations. Notably, the contribution of the inertial force becomes more evident as the input frequency increases. The dashed blue line in Fig. 8 (b) indicates that the inertance of the modeled IECD was 510 kg. In addition, a dynamic test on the designed IECD was conducted using an air gap $\Delta_3^2 = 5$ mm under sinusoidal excitation with an amplitude of 30 mm. Figure 9 shows a comparison of the test results obtained under this condition with sinusoidal excitations of 0.2 Hz and 0.5 Hz.

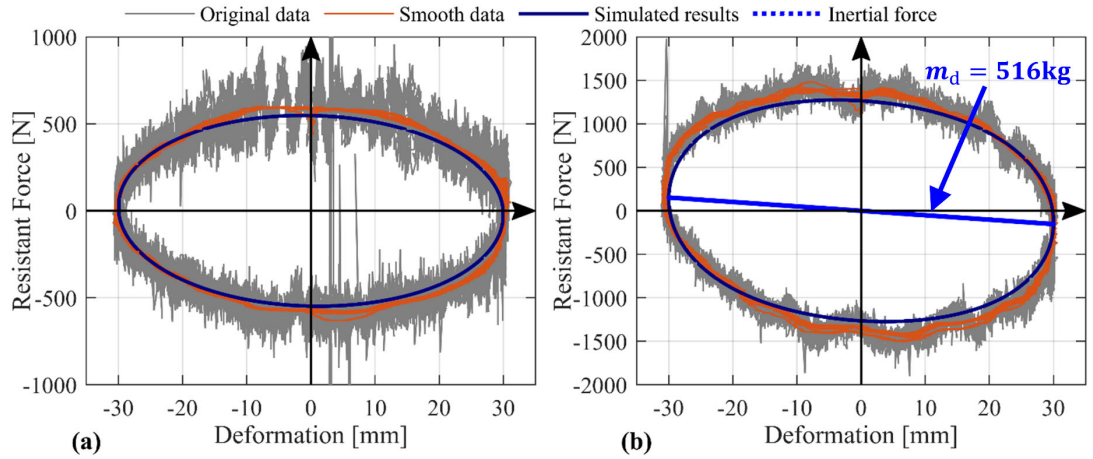

Fig. 9 Hysteretic loops of IECD under sinusoidal excitations of (a) 0.2 Hz and (b) 0.5 Hz (amplitude = 30 mm, $\Delta_3^2 = 5$ mm, and sampling rate = 1000 Hz).

Figure 9 shows that the approximate results correspond well with the smoothed test data, demonstrating that the proposed mechanical model can effectively estimate the mechanical behavior of the designed IECD. Furthermore, the identified inertance of the IECD was approximately 516 kg, which is nearly equal to the result identified for an air gap of 10 mm. The error between the experimentally observed inertance and the approximated inertance of 451

kg may be attributed to the existence of inertance in the ball screw and ball. As the inertance and finite stiffness of the fixture constitute an undesirable vibratory system, the local vibrations of the IECD and fixture gradually increase with the excitation frequency, resulting in the high-frequency noise observed in the hysteresis loops.

4.4 Equivalent formulation of eddy current damping

The relationship between the eddy current damping and equivalent linear viscous damping must be established to investigate the mechanical behavior of the IECD in a generalized manner. In this study, we assume that the electromagnetic field is quasistatic. Thus, given a sinusoidal excitation $u(t) = \tilde{u}\sin(\omega t)$ and $\dot{u}(t) = \omega\tilde{u}\cos(\omega t)$, the energy dissipation E_1 owing to the eddy current damping with the critical damping coefficients c_0 and critical velocity v_0 in a cycle can be expressed as

$$E_1 = 4\int_0^{\tilde{u}} c_0 \frac{v_0^2}{v_0^2+\dot{u}^2}\dot{u}\mathrm{d}u = 2c_0 v_0^2 \frac{\pi}{\omega}\left(1 - v_0/\sqrt{\tilde{u}^2\omega^2 + v_0^2}\right). \tag{28}$$

Meanwhile, the energy dissipation of the linear viscous damping can be computed as

$$E_2 = 4\int_0^{\tilde{u}} c_\mathrm{e}\dot{u}\mathrm{d}u = \pi\omega c_\mathrm{e}\tilde{u}^2. \tag{29}$$

By equating Eqs. (28) and (29), the equivalent damping coefficient of eddy current damping is given by

$$c_\mathrm{e} = \frac{2c_0}{\rho^2}\left(\frac{\sqrt{\rho^2+1}-1}{\sqrt{\rho^2+1}}\right), \quad \rho = \frac{\tilde{u}\omega}{v_0}. \tag{30}$$

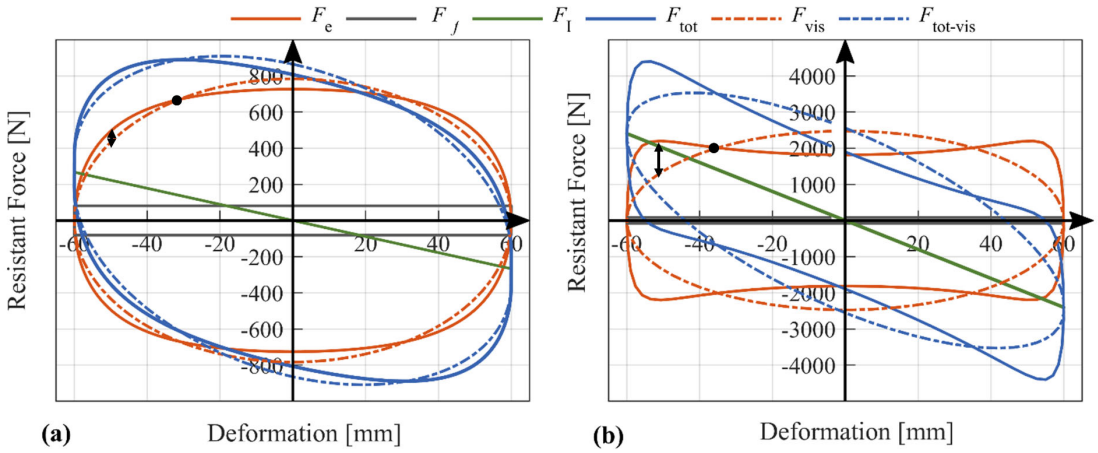

Fig. 10 Comparison of the mechanical model for the IECD and equivalent VMD under harmonic excitation with $\tilde{u} = 60$ mm and frequencies of (a) 0.5 Hz and (b) 1.5 Hz.

To illustrate Eqs. (28)–(30), Fig. 10 shows a comparison between the equivalent VMD and designed IECD under harmonic excitation with an amplitude of 60 mm at excitation frequencies of 0.5 Hz and 1.5 Hz. The equivalent viscous damping and total axial forces are represented by

F_{vis} and $F_{\mathrm{tot-vis}}$, respectively.

In Figs. 10 (a) and 10 (b), the solid and dash-dotted lines in orange denote the eddy current damping force and equivalent viscous damping force under harmonic excitation, respectively. Figure 10 (a) shows that the eddy current damping force approaches its peak when the velocity reaches its maximum under a harmonic excitation of 0.5 Hz. However, Fig. 10 (b) indicates that the peak eddy current damping force shifts away from zero displacement, implying that the eddy current damping is degraded when the input velocity exceeds v_0. This special characteristic of the eddy current damping may provide a fail-safe mechanism to prevent damage to the connecting part and the damper itself caused by excessive reaction forces generated by the device. Thus, the robustness of the structure equipped with the IECD device can be ensured. Furthermore, it was found that the amplitude of the eddy current damping force was larger than the equivalent viscous damping in the range between the peak displacements and the intersection points of the two damping models; this implies that the IECD is more effective than the equivalent VMD in dissipating earthquake energies at smaller velocities.

5 Optimal design of TIECD

In this section, the optimal design of the proposed TIECD is described. The resonance of the supplemental vibratory system used for tuning, comprising the spring connected in series to the IECD and the inerter element in the IECD connected to the primary structure, enhanced the energy dissipation afforded by the eddy current damper. Figure 11 presents a schematic of an SDOF structure equipped with the proposed TIECD.

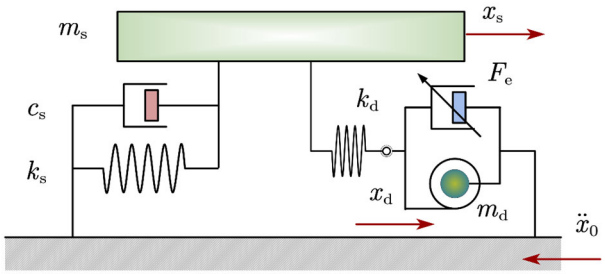

Fig. 11 SDOF structure equipped with TIECD.

5.1 Determination of TIECD parameters

The governing equations of an SDOF system equipped with a TIECD are given as

$$\begin{aligned} m_{\mathrm{s}}\ddot{x}_{\mathrm{s}} + c_{\mathrm{s}}\dot{x}_{\mathrm{s}} + k_{\mathrm{s}}x_{\mathrm{s}} + F_{\mathrm{d}} &= -m_{\mathrm{s}}\ddot{x}_0, \\ F_{\mathrm{d}} = m_{\mathrm{d}}\ddot{x}_{\mathrm{d}} + F_{\mathrm{e}} &= k_{\mathrm{d}}(x_{\mathrm{s}} - x_{\mathrm{d}}), \\ F_{\mathrm{e}} &= c_0\dot{x}_{\mathrm{d}}\, v_0^2/\left(v_0^2 + \dot{x}_{\mathrm{d}}^2\right), \end{aligned} \tag{31}$$

where m_{s}, c_{s}, and k_{s} denote the mass, damping coefficient, and stiffness of the SDOF system, respectively; m_{d} and k_{d} denote the inertance and supporting spring stiffness of the TIECD,

respectively. By employing the equivalence between the linear viscous damping force and eddy current damping force derived in Section 4.4, a dimensionless formulation can be expressed as

$$\begin{aligned} \ddot{x}_\mathrm{s} + 2\zeta_\mathrm{s}\omega_\mathrm{s}\dot{x}_\mathrm{s} + \omega_\mathrm{s}^2 x_\mathrm{s} + \mu_\mathrm{d}\gamma_\mathrm{d}^2\omega_\mathrm{s}^2(x_\mathrm{s} - x_\mathrm{d}) &= -\ddot{x}_0, \\ \mu_\mathrm{d}\ddot{x}_\mathrm{d} + 2\zeta_\mathrm{d}\omega_\mathrm{s}\dot{x}_\mathrm{d} + \mu_\mathrm{d}\gamma_\mathrm{d}^2\omega_\mathrm{s}^2(x_\mathrm{d} - x_\mathrm{s}) &= 0, \end{aligned} \tag{32}$$

where γ_d is the dimensionless frequency ratio, and ζ_d is the dimensionless damping ratio, as defined in the Nomenclature table.

Using the fixed-point-based optimization procedure [5] and the equivalent damping model defined in Section 4.4, an optimization procedure was developed to determine the TIECD parameters. According to Ikago, Saito, and Inoue [5], the optimal frequency ratio $\gamma_\mathrm{d}^{\mathrm{opt}}$ and optimal damping ratio $\zeta_\mathrm{d}^{\mathrm{opt}}$ of the equivalent TVMD can be obtained as functions of the mass ratio μ_d, as follows:

$$\gamma_\mathrm{d}^{\mathrm{opt}} = 1/\sqrt{1-\mu_\mathrm{d}}, \tag{33}$$

$$\zeta_\mathrm{d}^{\mathrm{opt}} = \frac{\mu_\mathrm{d}}{2}\sqrt{\frac{3\mu_\mathrm{d}}{(1-\mu_\mathrm{d})(2-\mu_\mathrm{d})}}. \tag{34}$$

Subsequently, the TIECD stiffness is obtained as $k_\mathrm{d} = \mu_\mathrm{d}(\gamma_\mathrm{d}^{\mathrm{opt}})^2 k_\mathrm{s}$ [5]. The optimal $c_\mathrm{e}^{\mathrm{opt}}$ of TIECD can then be computed using the equivalent relationship expressed in Eq. (30), using a given v_0. The complex eigenvector was obtained from a complex eigenanalysis of the structure equipped with the equivalent TVMD. Given the target inter-story drift of the SDOF system $x_\mathrm{s}^{\max}$ and the corresponding deformation of the IECD $x_\mathrm{d}^{\max}$, the threshold velocity responses $\dot{x}_\mathrm{s}^{\max}$ and $\dot{x}_\mathrm{d}^{\max}$ can be approximated as

$$\dot{x}_\mathrm{s}^{\max} = \omega_1 x_\mathrm{s}^{\max} \quad \dot{x}_\mathrm{d}^{\max} = \omega_1 x_\mathrm{d}^{\max}, \tag{35}$$

where ω_1 denotes the fundamental natural frequency obtained from the complex eigenanalysis. The threshold velocity of the IECD $\dot{x}_\mathrm{d}^{\max}$ is proportional to v_0, that is, $\dot{x}_\mathrm{d}^{\max} = \kappa v_0$. When $\kappa < 1$, the maximum velocity response is smaller than the designed v_0, indicating that the damping force is always in the ascending interval of the backbone curve of the eddy current damping. Otherwise, the maximum velocity is larger than v_0, and the ultimate damping force is smaller than the maximum damping force. In this case, the proportional relationship among the components in the complex eigenvector $\boldsymbol{\phi} = [\phi_\mathrm{s}, \phi_\mathrm{d}]^\mathrm{T}$ can be adopted to determine the value of v_0 for the IECD, as follows:

$$\frac{|\phi_\mathrm{s}|}{|\phi_\mathrm{d}|} = \frac{x_\mathrm{s}^{\max}}{x_\mathrm{d}^{\max}} = \frac{\dot{x}_\mathrm{s}^{\max}}{\dot{x}_\mathrm{d}^{\max}} \Rightarrow v_0 = \frac{\omega_1 x_\mathrm{s}^{\max}|\phi_\mathrm{d}|}{\kappa|\phi_\mathrm{s}|} = \frac{\omega_1 x_\mathrm{d}^{\max}}{\kappa}. \tag{36}$$

By letting $\rho = \kappa$ and substituting Eq. (36) into Eq. (30), the designed c_0 of the TIECD can be determined by

$$c_0 = \frac{c_\mathrm{e}}{2}\left(\kappa^2 + 1 + \sqrt{\kappa^2+1}\right). \tag{37}$$

A design flow chart for the TIECD is shown in Fig. 12.

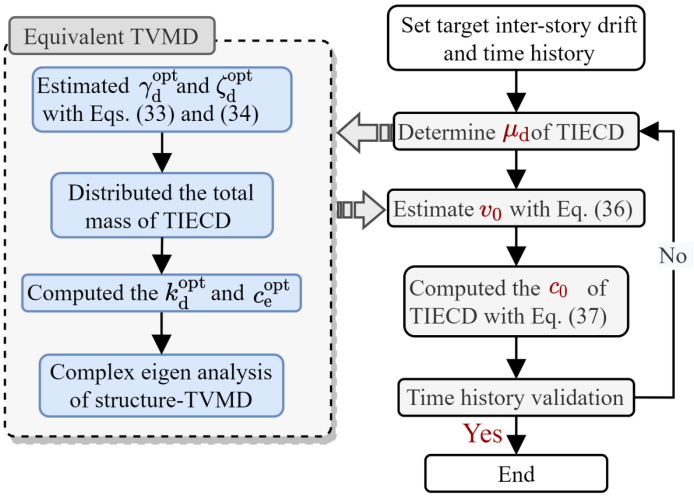

Fig. 12 Flowchart of design procedure for TIECD.

5.2 Shake table validation of TIECD

The SDOF steel structure specimen, shown in Fig. 13, was used to experimentally examine the control effect of the designed TIECD. To avoid damage to the leaf spring columns, the maximum drift of the specimens was limited to 20 mm. Basic information related to the SDOF steel structure specimens can be found in [5]. The fundamental natural period of the specimen was 0.56 s, and the time step interval of the input ground motion was compressed to half of the original data to simulate a structure whose fundamental natural frequency was close to 1 s. Table 3 lists the optimal parameters of the TIECD, obtained for the given apparent mass of 451 kg, target inter-story drift x_s^{max} of 13 mm, and ratio of modification factor κ of unity.

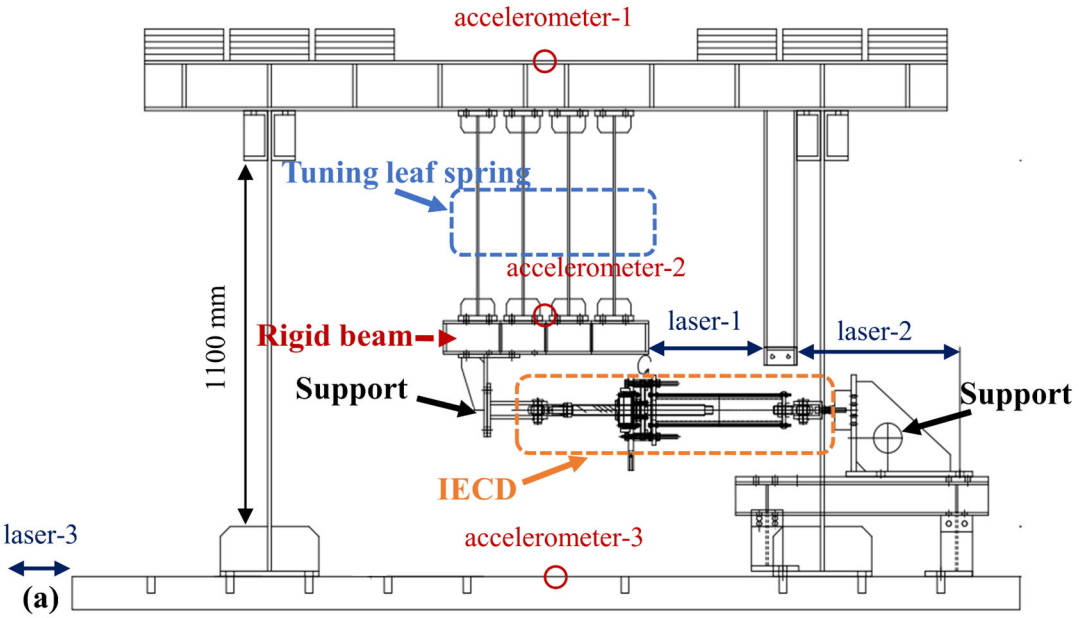

(b)

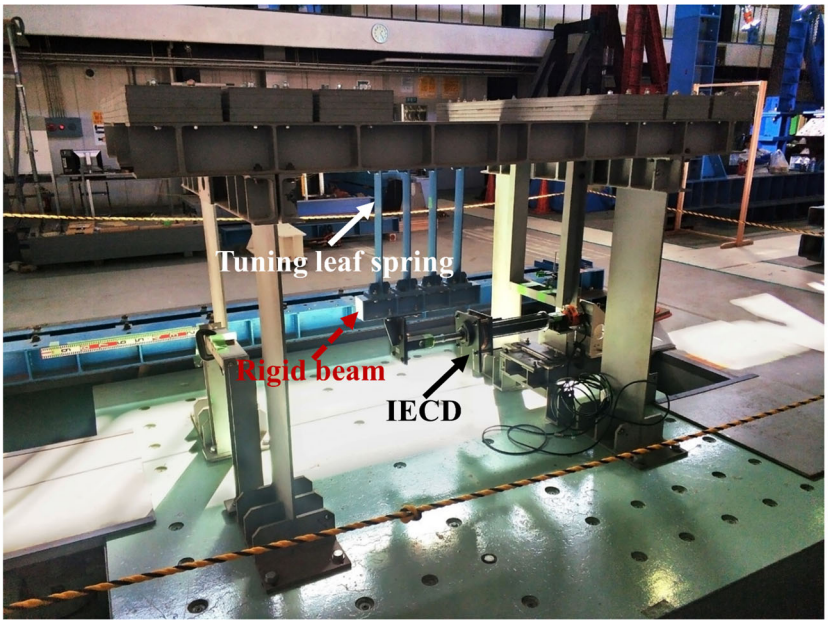

Fig. 13 (a) Schematic and (b) photograph of the TIECD test.

Table 3 Optimized parameters of designed TIECD

Parameters	Optimized value
$\gamma_{\mathrm{d}}^{\mathrm{opt}}$	1.12
$\zeta_{\mathrm{d}}^{\mathrm{opt}}$	0.067
$k_{\mathrm{e}}^{\mathrm{opt}}$	72.4 [kN/m]
$c_{\mathrm{e}}^{\mathrm{opt}}$	3344 [N · s/m]
c_0^{opt}	5708 [N · s/m]
v_0^{opt}	0.320 [m/s]

Unlike the TVMD systems applied to real-world buildings, in which natural rubber is used as a supporting spring device [86,87], we used a set of soft-leaf springs as the spring element to tune the frequency of the designed TIECD. As illustrated in Fig. 13, the tested TIECD was constructed by connecting the proposed IECD to four soft-leaf springs with a rigid beam. For the TIECD specimen used in the test, the stiffness of the tuning leaf spring $k_{\mathrm{e}} = 95\,\mathrm{kN/m}$, $v_0 = 0.309\,\mathrm{m/s}$, $c_0 = 5286\,\mathrm{N \cdot s/m}$, and $\tilde{F}_{\mathrm{f}} = 81\,\mathrm{N}$. The equivalent damping coefficient was estimated from the sum of the eddy current damping and friction forces. The equivalent linear damping coefficient of the friction force was estimated as follows:

$$c_{\mathrm{e,f}} = \frac{4\tilde{F}_{\mathrm{f}}}{\pi \dot{x}_{\mathrm{d}}^{\max}} = 323\,\mathrm{N \cdot s/m}. \tag{38}$$

According to Eq. (30), the ratio ρ was estimated as

$$\rho = \omega_1 x_{\mathrm{d}}^{\max}/v_0 = 0.32/0.309 = 1.035, \tag{39}$$

and the contribution of eddy current damping force was computed as

$$c_{\mathrm{e}} = \frac{2c_0}{\rho^2}\left(\frac{\sqrt{\rho^2+1}-1}{\sqrt{\rho^2+1}}\right) = 3011\,\mathrm{N \cdot s/m}. \tag{40}$$

Therefore, the total equivalent damping coefficient of $3334\,\mathrm{N \cdot s/m}$ was nearly equal to $c_{\mathrm{e}}^{\mathrm{opt}}$.

The ground motion record of the 1940 Imperial Valley Earthquake, as recorded at the El Centro station, was then used to evaluate the control effect of the TIECD, which was reduced to 80% of its original magnitude to ensure that the maximum response displacement of the steel structure specimen remained within the allowable limits. A comparison of the numerical simulation and experimental results for the story drift and deformation of the IECD is presented in Fig. 14. Additionally, the numerical simulation results of a similar system equipped with an equivalent TVMD using a tuning spring identical to that of the proposed TIECD are plotted for further comparison.

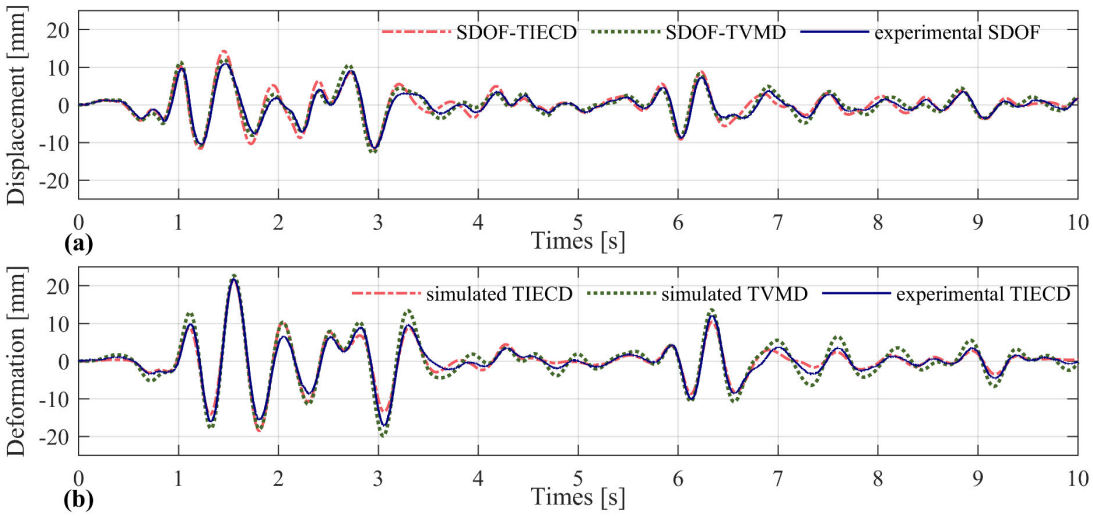

Fig. 14 Comparison of simulated results and experimental data for (a) drift of the primary structure and (b) deformation of TIECD and TVMD.

Figure 14 shows that the simulated displacement response of the primary structure nearly overlaps with the experimental observations, thus demonstrating the accuracy of the proposed TIECD simulation model. Furthermore, the well-matched displacement responses obtained from the TIECD and equivalent TVMD systems indicate that the proposed equivalent linearization model of the IECD effectively captures the relationship between the eddy current damping force and viscous damping force. In addition to the comparisons of the displacement responses and relationships between the damping force, the “damping enhancement” effect [72] can be observed on comparing Figs. 14 (a) and 14 (b). This indicates that the maximum displacement response of the IECD was considerably larger than that of the primary structure. To clarify the “damping enhancement” effect of the designed TIECD, a numerical simulation of the SDOF system equipped with an IECD was also conducted, and detailed comparisons of the resulting hysteretic damping force loops and energy dissipations are shown in Figs. 15 (a) and 15 (b), respectively.

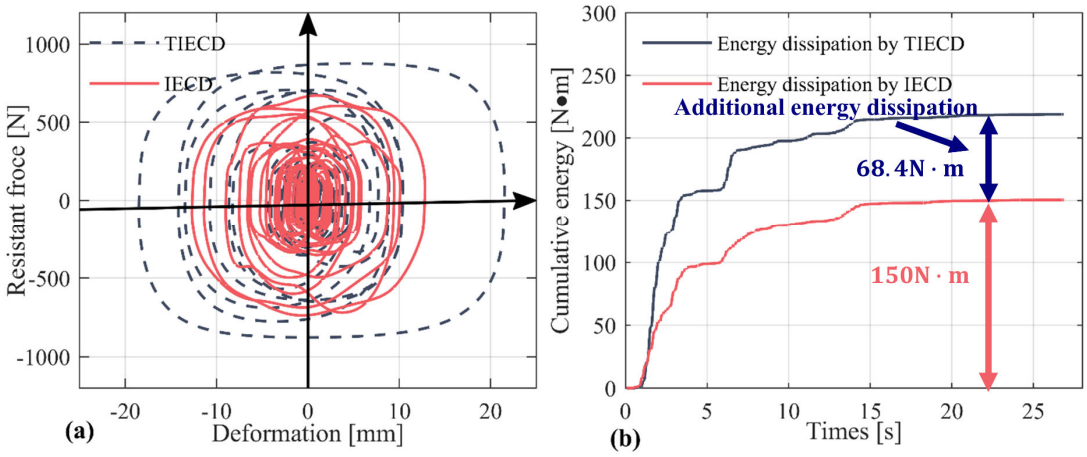

Fig. 15 Comparison of (a) hysteretic loops of damping force and (b) energy dissipations of IECD and TIECD.

As shown in Fig. 15, the damping forces of the TIECD and IECD consist of friction and eddy current damping forces. Fig. 15 (a) shows that the energy dissipation is enhanced on attaching a tuned stiffness spring component, rendering the hysteretic loop of the TIECD considerably larger than that of the IECD. The additional energy dissipation in Fig. 15 (b) demonstrates that the increase in energy dissipation afforded by the TIECD was half that of the original IECD.

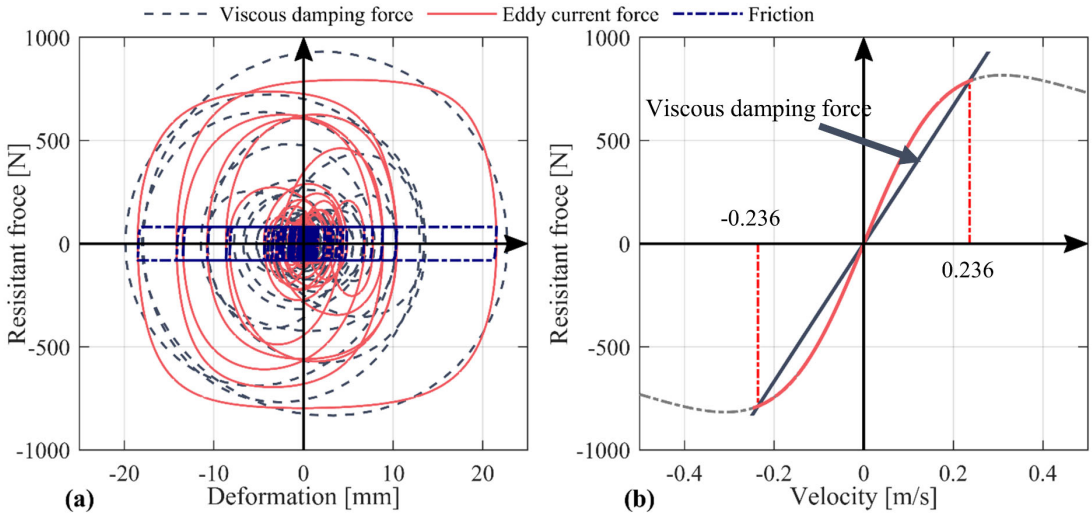

Fig. 16 (a) Hysteretic loop of damping force and (b) relationship between eddy current damping force and input velocity of TIECD.

Figure 16 (a) compares the hysteretic loops of the damping parts of the TIECD and equivalent TVMD. The simulated TIECD can be observed to provide a hysteretic loop comparable to that for the equivalent viscous damping. It is noteworthy that eddy current damping provides a larger damping force than equivalent viscous damping at velocities less than 0.236 m/s, as this implies that the eddy current damping mechanism is more efficient across a smaller velocity range than the classical linear viscous damping model. Additionally, the degradation of the damping force

for input velocities greater than v_0 may serve as a fail-safe mechanism to protect the device connecting the primary structure components.

6 Conclusions and remarks

This study investigated a mechanical model and the optimal design of a dynamic vibration absorber for use in civil structures, namely the TIECD. The proposed TIECD employs the inertance and electromagnetic damping produced by rotating back iron disks attached to the permanent magnets and eddy currents, respectively. The SVM method was first used to estimate the equivalent eddy current damping force of the IECD, by employing a succinct two-parameter fitting model that described its nonlinear behavior. Subsequently, an experimental evaluation of a small-scale IECD was conducted to validate the effectiveness and accuracy of the proposed electromagnetic equations and fitting model. As expected, the well-matched experimental results demonstrated the effectiveness of the proposed model. An equivalent damping coefficient for eddy current damping was then derived to explore the energy dissipation ability in a generalized manner. Furthermore, an optimal design procedure for TIECD was established using a combination of the equivalent damping model, fixed-point optimization method, and complex eigenanalysis. Finally, a shake table test was conducted to evaluate the control effect of the TIECD on an SDOF benchmark model. The observed agreement between the simulated results and experimental observations confirmed that the designed TIECD could control the system response with a high efficiency. Additionally, the "damping enhancement" effect of the TIECD was observed. This indicated that the displacement responses of the IECD were considerably larger than those of the primary structure, resulting in enhanced energy dissipation by the eddy currents. Thus, the characteristics of the eddy current damping force, namely the high damping coefficient in the low-speed range and the low damping coefficient in the high-speed range, may help ensure the structural control effect by protecting secondary components from possible damage caused by extremely strong earthquake excitations.

Acknowledgments

We would like to thank Editage (http://www.editage.com) for editing and reviewing this manuscript for the English language.

Funding:

This study was supported by a Grant-in-Aid from the Japan Society for the Promotion of Science, Grant/Award Number: JSPS KAKENHI [grant number 18F18761].

References

[1] M.C. Smith, Synthesis of mechanical networks the inerter, IEEE Transactions on Automatic Control. 47 (2002) 1648–1662. https://doi.org/10.1109/TAC.2002.803532.

[2] Kawaguchi O., Kanoh T., Akino K., Kato M., Sunakoda K., Research and development of seismic restraint snubbers. (I)., Journal of the Atomic Energy Society of Japan / Atomic Energy Society of Japan. 33 (1991) 76–89. https://doi.org/10.3327/jaesj.33.76.

[3] Y. Shen, L. Chen, X. Yang, D. Shi, J. Yang, Improved design of dynamic vibration absorber by using the inerter and its application in vehicle suspension, Journal of Sound and Vibration. 361 (2016) 148–158. https://doi.org/10.1016/j.jsv.2015.06.045.

[4] F.-C. Wang, M.-K. Liao, The lateral stability of train suspension systems employing inerters, Vehicle System Dynamics. 48 (2010) 619–643. https://doi.org/10.1080/00423110902993654.

[5] K. Ikago, K. Saito, N. Inoue, Seismic control of single-degree-of-freedom structure using tuned viscous mass damper, Earthquake Engineering & Structural Dynamics. 41 (2012) 453–474. https://doi.org/10.1002/eqe.1138.

[6] K. Ikago, Y. Sugimura, K. Saito, N. Inoue, Modal Response Characteristics of a Multiple-Degree-Of-Freedom Structure Incorporated with Tuned Viscous Mass Dampers, Journal of Asian Architecture and Building Engineering. 11 (2012) 375–382. https://doi.org/10.3130/jaabe.11.375.

[7] I. Takewaki, S. Murakami, S. Yoshitomi, M. Tsuji, Fundamental mechanism of earthquake response reduction in building structures with inertial dampers, Structural Control and Health Monitoring. 19 (2012) 590–608. https://doi.org/10.1002/stc.457.

[8] M. Saitoh, On the performance of gyro-mass devices for displacement mitigation in base isolation systems, Struct. Control Health Monit. 19 (2012) 246–259. https://doi.org/10.1002/stc.419.

[9] I.F. Lazar, S.A. Neild, D.J. Wagg, Using an inerter-based device for structural vibration suppression, Earthquake Engineering & Structural Dynamics. 43 (2014) 1129–1147. https://doi.org/10.1002/eqe.2390.

[10] N. Makris, G. Kampas, Seismic Protection of Structures with Supplemental Rotational Inertia, Journal of Engineering Mechanics. 142 (2016) 04016089. https://doi.org/10.1061/(ASCE)EM.1943-7889.0001152.

[11] R. Zhang, Z. Zhao, C. Pan, Influence of mechanical layout of inerter systems on seismic mitigation of storage tanks, Soil Dynamics and Earthquake Engineering. 114 (2018) 639–649. https://doi.org/10.1016/j.soildyn.2018.07.036.

[12] A.A. Taflanidis, A. Giaralis, D. Patsialis, Multi-objective optimal design of inerter-based vibration absorbers for earthquake protection of multi-storey building structures, Journal of the Franklin Institute. 356 (2019) 7754–7784. https://doi.org/10.1016/j.jfranklin.2019.02.022.

[13] R. Zhang, Z. Zhao, K. Dai, Seismic response mitigation of a wind turbine tower using a tuned parallel inerter mass system, Engineering Structures. 180 (2019) 29–39. https://doi.org/10.1016/j.engstruct.2018.11.020.

[14] Z. Huang, X. Hua, Z. Chen, H. Niu, Optimal design of TVMD with linear and nonlinear viscous damping for SDOF systems subjected to harmonic excitation, Struct Control Health Monit. 26 (2019) e2413. https://doi.org/10.1002/stc.2413.

[15] W. Shen, A. Niyitangamahoro, Z. Feng, H. Zhu, Tuned inerter dampers for civil structures subjected to earthquake ground motions: optimum design and seismic performance, Engineering Structures. 198 (2019) 109470. https://doi.org/10.1016/j.engstruct.2019.109470.

[16] S. Kawamata, M. Yoneda, Y. Hangai, Development of Vibration Control System for Structures by Means of Mass Pumps, Seisan Kenkyu. 26 (1974) 431–436.

[17] Y. Shen, Y. Liu, L. Chen, X. Yang, Optimal design and experimental research of vehicle suspension based on a hydraulic electric inerter, Mechatronics. 61 (2019) 12–19. https://doi.org/10.1016/j.mechatronics.2019.05.002.

[18] D. De Domenico, P. Deastra, G. Ricciardi, N.D. Sims, D.J. Wagg, Novel fluid inerter based tuned mass dampers for optimised structural control of base-isolated buildings, Journal of the Franklin Institute. 356 (2018) 7626–7649. https://doi.org/10.1016/j.jfranklin.2018.11.012.
[19] D. De Domenico, G. Ricciardi, R. Zhang, Optimal design and seismic performance of tuned fluid inerter applied to structures with friction pendulum isolators, Soil Dynamics and Earthquake Engineering. 132 (2020) 106099. https://doi.org/10.1016/j.soildyn.2020.106099.
[20] C. Papageorgiou, N.E. Houghton, M.C. Smith, Experimental Testing and Analysis of Inerter Devices, Journal of Dynamic Systems, Measurement, and Control. 131 (2009) 011001. https://doi.org/10.1115/1.3023120.
[21] R. Mirza Hessabi, O. Mercan, Investigations of the application of gyro-mass dampers with various types of supplemental dampers for vibration control of building structures, Engineering Structures. 126 (2016) 174–186. https://doi.org/10.1016/j.engstruct.2016.07.045.
[22] A. Gonzalez-Buelga, L.R. Clare, S.A. Neild, J.Z. Jiang, D.J. Inman, An electromagnetic inerter-based vibration suppression device, Smart Materials and Structures. 24 (2015) 1–10. https://doi.org/10.1088/0964-1726/24/5/055015.
[23] D. Konstantinidis, N. Makris, J.M. Kelly, In-situ condition assessment of seismic fluid dampers: experimental studies and challenges, Meccanica. 50 (2015) 323–340. https://doi.org/10.1007/s11012-014-9882-4.
[24] H.D. Wiederick, N. Gauthier, D.A. Campbell, P. Rochon, Magnetic braking: Simple theory and experiment, American Journal of Physics. 55 (1987) 500–503. https://doi.org/10.1119/1.15103.
[25] J.H. Wouterse, Critical torque and speed of eddy current brake with widely separated soft iron poles, IEE Proc. B Electr. Power Appl. UK. 138 (1991) 153–158. https://doi.org/10.1049/ip-b.1991.0019.
[26] C.S. MacLatchy, P. Backman, L. Bogan, A quantitative magnetic braking experiment, American Journal of Physics. 61 (1993) 1096–1101. https://doi.org/10.1119/1.17356.
[27] K.E. Graves, D. Toncich, P.G. Iovenitti, THEORETICAL COMPARISON OF MOTIONAL AND TRANSFORMER EMF DEVICE DAMPING EFFICIENCY, Journal of Sound and Vibration. 233 (2000) 441–453. https://doi.org/10.1006/jsvi.1999.2820.
[28] H.A. Sodano, J.-S. Bae, D.J. Inman, W. Keith Belvin, Concept and model of eddy current damper for vibration suppression of a beam, Journal of Sound and Vibration. 288 (2005) 1177–1196. https://doi.org/10.1016/j.jsv.2005.01.016.
[29] H.A. Sodano, J.-S. Bae, D.J. Inman, W.K. Belvin, Improved Concept and Model of Eddy Current Damper, Transactions of the ASME. 128 (2006) 294–302. https://doi.org/10.1115/1.2172256.
[30] A. Tonoli, Dynamic characteristics of eddy current dampers and couplers, Journal of Sound and Vibration. 301 (2007) 576–591. https://doi.org/10.1016/j.jsv.2006.10.015.
[31] A. Canova, B. Vusini, Design of axial eddy-current couplers, IEEE Transactions on Industry Applications. 39 (2003) 725–733. https://doi.org/10.1109/TIA.2003.811783.
[32] J. Wang, H. Lin, S. Fang, Y. Huang, A General Analytical Model of Permanent Magnet Eddy Current Couplings, IEEE Transactions on Magnetics. 50 (2014) 1–9. https://doi.org/10.1109/TMAG.2013.2279073.
[33] Z.W. Huang, X.G. Hua, Z.Q. Chen, H.W. Niu, Modeling, Testing, and Validation of an Eddy Current Damper for Structural Vibration Control, Journal of Aerospace Engineering. 31 (2018) 04018063. https://doi.org/10.1061/(asce)as.1943-5525.0000891.
[34] S. Li, Y. Li, J. Wang, Z. Chen, Theoretical investigations on the linear and nonlinear damping force for an eddy current damper combining with rack and gear, Journal of Vibration and Control. (2021) 107754632098778. https://doi.org/10.1177/1077546320987787.
[35] Y. Nakamura, A. Fukukita, K. Tamura, I. Yamazaki, T. Matsuoka, K. Hiramoto, K. Sunakoda, Seismic response control using electromagnetic inertial mass dampers, Earthquake Engineering & Structural Dynamics. 43 (2014) 507–527. https://doi.org/10.1002/eqe.2355.
[36] T. Asai, Y. Araki, K. Ikago, Energy harvesting potential of tuned inertial mass electromagnetic transducers, Mechanical Systems and Signal Processing. 84 (2017) 659–672. https://doi.org/10.1016/j.ymssp.2016.07.048.
[37] H. Zhu, Y. Li, W. Shen, S. Zhu, Mechanical and energy-harvesting model for

electromagnetic inertial mass dampers, Mechanical Systems and Signal Processing. 120 (2019) 203–220. https://doi.org/10.1016/j.ymssp.2018.10.023.
[38] W. Shen, Z. Sun, Y. Hu, L. Cai, H. Zhu, S. Silva, Energy harvesting performance of an inerter-based electromagnetic damper with application to stay cables, Mechanical Systems and Signal Processing. 170 (2022) 108790. https://doi.org/10.1016/j.ymssp.2021.108790.
[39] K. Karakoc, A. Suleman, E.J. Park, Analytical modeling of eddy current brakes with the application of time varying magnetic fields, Applied Mathematical Modelling. 40 (2016) 1168–1179. https://doi.org/10.1016/j.apm.2015.07.006.
[40] T. Szmidt, D. Pisarski, R. Konowrocki, Semi-active stabilisation of a pipe conveying fluid using eddy-current dampers: state-feedback control design, experimental validation, Meccanica. 54 (2019) 761–777. https://doi.org/10.1007/s11012-019-00988-3.
[41] W. Bähler, W. van der Hoek, An eddy-current coupling employed as a variable-speed drive, PHILIPS TECHNICAL REVIEW. 1 (1966) 15–21.
[42] A. Wallace, A. von Jouanne, Industrial speed control: are PM couplings an alternative to VFDs?, IEEE Industry Applications Magazine. 7 (2001) 57–63. https://doi.org/10.1109/2943.948533.
[43] T. Lubin, A. Rezzoug, Steady-State and Transient Performance of Axial-Field Eddy-Current Coupling, IEEE Transactions on Industrial Electronics. 62 (2015) 2287–2296. https://doi.org/10.1109/TIE.2014.2351785.
[44] W. Li, D. Wang, D. Kong, S. Wang, Z. Hua, A novel method for modeling the air gap flux density of the axial-flux permanent magnet eddy current coupler considering the end-effect, Energy Reports. 7 (2021) 508–514. https://doi.org/10.1016/j.egyr.2021.08.012.
[45] C. Yu, Z. Deng, L. Mei, C. Peng, X. Cao, Multiobjective optimization of 3-DOF magnetic bearing considering eddy current effects and saturation, Mechanical Systems and Signal Processing. 182 (2023) 109538. https://doi.org/10.1016/j.ymssp.2022.109538.
[46] J.G. Detoni, Q. Cui, N. Amati, A. Tonoli, Modeling and evaluation of damping coefficient of eddy current dampers in rotordynamic applications, Journal of Sound and Vibration. 373 (2016) 52–65. https://doi.org/10.1016/j.jsv.2016.03.013.
[47] L. Ye, C. Liang, Y. Liu, D. Li, Z. Liu, Performance analysis and test of a novel eddy-current braking & heating system for electric bus, Energy Conversion and Management. 183 (2019) 440–449. https://doi.org/10.1016/j.enconman.2019.01.010.
[48] B. Kou, W. Chen, Y. Jin, A Novel Cage-Secondary Permanent Magnet Linear Eddy Current Brake With Wide Speed Range and its Analytical Model, IEEE Trans. Ind. Electron. 69 (2022) 7130–7139. https://doi.org/10.1109/TIE.2021.3097603.
[49] Z. Wang, Z. Chen, J. Wang, Feasibility study of a large-scale tuned mass damper with eddy current damping mechanism, Earthquake Engineering and Engineering Vibration. 11 (2012) 391–401. https://doi.org/10.1007/s11803-012-0129-x.
[50] Q. Wen, X.G. Hua, Z.Q. Chen, Y. Yang, H.W. Niu, Control of Human-Induced Vibrations of a Curved Cable-Stayed Bridge: Design, Implementation, and Field Validation, J. Bridge Eng. 21 (2016) 04016028. https://doi.org/10.1061/(ASCE)BE.1943-5592.0000887.
[51] L. Irazu, M.J. Elejabarrieta, Analysis and numerical modelling of eddy current damper for vibration problems, Journal of Sound and Vibration. 426 (2018) 75–89. https://doi.org/10.1016/j.jsv.2018.03.033.
[52] X. Lu, Q. Zhang, D. Weng, Z. Zhou, S. Wang, S.A. Mahin, S. Ding, F. Qian, Improving performance of a super tall building using a new eddy-current tuned mass damper, Structural Control and Health Monitoring. 24 (2017) e1882. https://doi.org/10.1002/stc.1882.
[53] L. Wang, W. Shi, X. Li, Q. Zhang, Y. Zhou, An adaptive-passive retuning device for a pendulum tuned mass damper considering mass uncertainty and optimum frequency, Struct Control Health Monit. 26 (2019) e2377. https://doi.org/10.1002/stc.2377.
[54] X. Lu, Q. Zhang, W. Wu, J. Shan, Data-Driven Two-Level Performance Evaluation of Eddy-Current Tuned Mass Damper for Building Structures Using Shaking Table and Field Testing, Computer-Aided Civil and Infrastructure Engineering. 34 (2019) 38–57. https://doi.org/10.1111/mice.12373.
[55] S. Liu, Z. Lu, P. Li, S. Ding, F. Wan, Shaking table test and numerical simulation of eddy-current tuned mass damper for structural seismic control considering soil-structure

interaction, Engineering Structures. 212 (2020) 110531. https://doi.org/10.1016/j.engstruct.2020.110531.
[56] Z. Shi, J. Shan, C.N. Loong, W. Wu, C.-C. Chang, W. Shi, Experimental and Numerical Study on Dynamic Behavior of Eddy Current Damping with Frequency Dependence, J. Eng. Mech. 146 (2020) 04020116. https://doi.org/10.1061/(ASCE)EM.1943-7889.0001852.
[57] M. Liu, S. Li, T. Wu, Y. Li, H. Meng, Z. Chen, Eddy-Current Tuned Mass Dampers for Mitigation of Wind-Induced Response of the Noor III Solar Tower: Design, Installation, and Validation, J. Struct. Eng. 147 (2021) 05021009. https://doi.org/10.1061/(ASCE)ST.1943-541X.0003180.
[58] M. Berardengo, A. Cigada, F. Guanziroli, S. Manzoni, Modelling and control of an adaptive tuned mass damper based on shape memory alloys and eddy currents, Journal of Sound and Vibration. 349 (2015) 18–38. https://doi.org/10.1016/j.jsv.2015.03.036.
[59] A. Asghar Maddah, Y. Hojjat, M. Reza Karafi, M. Reza Ashory, Reduction of magneto rheological dampers stiffness by incorporating of an eddy current damper, Journal of Sound and Vibration. 396 (2017) 51–68. https://doi.org/10.1016/j.jsv.2017.02.011.
[60] M. Amjadian, A.K. Agrawal, Modeling, design, and testing of a proof-of-concept prototype damper with friction and eddy current damping effects, Journal of Sound and Vibration. 413 (2018) 225–249. https://doi.org/10.1016/j.jsv.2017.10.025.
[61] M. Amjadian, A.K. Agrawal, Feasibility study of using a semiactive electromagnetic friction damper for seismic response control of horizontally curved bridges, Struct Control Health Monit. 26 (2019) e2333. https://doi.org/10.1002/stc.2333.
[62] H.Y. Zhang, Z.Q. Chen, X.G. Hua, Z.W. Huang, H.W. Niu, Design and dynamic characterization of a large-scale eddy current damper with enhanced performance for vibration control, Mechanical Systems and Signal Processing. 145 (2020) 106879. https://doi.org/10.1016/j.ymssp.2020.106879.
[63] L. Liang, Z. Feng, Z. Chen, Seismic Control of SDOF Systems with Nonlinear Eddy Current Dampers, Applied Sciences. 9 (2019) 1–18. https://doi.org/10.3390/app9163427.
[64] Z. Wang, Z. Cheng, H. Wang, F. Yue, H. Gao, B. Fan, Damping of a stay cable with two eddy-current inertial mass dampers: Theoretical analysis, experimental study, and parameter optimization, Structural Contr & Hlth. e3085 (2022) 1–23. https://doi.org/10.1002/stc.3085.
[65] J.-Y. Li, S. Zhu, J. Shen, Enhance the damping density of eddy current and electromagnetic dampers, Smart Structures and Systems. 24 (2019) 15–26. https://doi.org/10.12989/sss.2019.24.1.015.
[66] Y. Li, S. Li, J. Wang, Z. Chen, A new type of damper combining eddy current damping with rack and gear, Journal of Vibration and Control. 0 (2020) 1–11. https://doi.org/10.1177/1077546320937110.
[67] S. Li, Y. Li, W. Mao, J. Wang, Z. Chen, A novel 500 kN axial eddy current damper using rack and gear mechanism: Design, testing, and evaluation, Structural Contr & Hlth. 29 (2022) 1–15. https://doi.org/10.1002/stc.3022.
[68] H. Sun, L. Zuo, X. Wang, J. Peng, W. Wang, Exact H_2 optimal solutions to inerter-based isolation systems for building structures, Structural Control and Health Monitoring. 26 (2019) e2357. https://doi.org/10.1002/stc.2357.
[69] L. Marian, A. Giaralis, Optimal design of a novel tuned mass-damper–inerter (TMDI) passive vibration control configuration for stochastically support-excited structural systems, Probabilistic Engineering Mechanics. 38 (2014) 156–164. https://doi.org/10.1016/j.probengmech.2014.03.007.
[70] D. Pietrosanti, M. De Angelis, M. Basili, Optimal design and performance evaluation of systems with Tuned Mass Damper Inerter (TMDI), Earthquake Engineering & Structural Dynamics. 46 (2017) 1367–1388. https://doi.org/10.1002/eqe.2861.
[71] D. De Domenico, G. Ricciardi, Optimal design and seismic performance of tuned mass damper inerter (TMDI) for structures with nonlinear base isolation systems, Earthquake Engineering & Structural Dynamics. 47 (2018) 2539–2560. https://doi.org/10.1002/eqe.3098.
[72] R. Zhang, Q. Zhao Zhipeng, C. Pan, K. Ikago, S. Xue, Damping enhancement principle of inerter system, Structural Control and Health Monitoring. 27 (2020) e2523.

https://doi.org/10.1002/stc.2523.
[73] R. Zhang, L. Zhang, C. Pan, D. De Domenico, Q. Chen, Targeted modal response control of structures using inerter systems based on master oscillator principle, International Journal of Mechanical Sciences. 206 (2021) 106636. https://doi.org/10.1016/j.ijmecsci.2021.106636.
[74] H. Wang, W. Yu, Rotary eddy current tuned mass damper, 2020.
[75] T. Szmidt, R. Konowrocki, D. Pisarski, Active eddy current device for damping torsional vibration in rotary motion, 2022.
[76] S. Mohammadi, M. Mirsalim, S. Vaez-Zadeh, H.A. Talebi, Analytical Modeling and Analysis of Axial-Flux Interior Permanent-Magnet Couplers, IEEE Transactions on Industrial Electronics. 61 (2014) 5940–5947. https://doi.org/10.1109/TIE.2014.2311391.
[77] J. Wang, J. Zhu, A Simple Method for Performance Prediction of Permanent Magnet Eddy Current Couplings Using a New Magnetic Equivalent Circuit Model, IEEE Transactions on Industrial Electronics. 65 (2018) 2487–2495. https://doi.org/10.1109/TIE.2017.2739704.
[78] R.L. Russell, K.H. Norsworthy, Eddy currents and wall losses in screened-rotor induction motors, Proceedings of the IEE Part A: Power Engineering. 105 (1958) 163–175. https://doi.org/10.1049/pi-a.1958.0036.
[79] D. Meeker, Finite element method magnetics, FEMM. (2019). http://www.femm.info/wiki/HomePage.
[80] R.L. Norton, Machine Design An Integrated Approach, 6th ed., Pearson Education, Inc., Hoboken, NJ 07030, 2020.
[81] F.-C. Wang, W.-J. Su, Impact of inerter nonlinearities on vehicle suspension control, Vehicle System Dynamics. 46 (2008) 575–595. https://doi.org/10.1080/00423110701519031.
[82] E.P. Furlani, Permanent magnet and electromechanical devices: materials, analysis, and applications, Academic press, San Diego, 2001.
[83] T. Lubin, A. Rezzoug, Improved 3-D Analytical Model for Axial-Flux Eddy-Current Couplings With Curvature Effects, IEEE Transactions on Magnetics. 53 (2017) 1–9. https://doi.org/10.1109/TMAG.2017.2714628.
[84] The Sage Developers, SageMath, (2019). https://www.sagemath.org.
[85] S. Sharif, J. Faiz, K. Sharif, Performance analysis of a cylindrical eddy current brake, IET Electr. Power Appl. 6 (2012) 661–668. https://doi.org/10.1049/iet-epa.2012.0006.
[86] Y. Sugimura, W. Goto, H. Tanizawa, K. Saito, T. Nimomiya, Response control effect of steel building structure using tuned viscous mass damper, in: 15th World Conference of Earthquake Engineering, Lisbon, Portugal, 2012: pp. 24–28.
[87] M. Ogino, T. Sumiyama, Structural Design of a High-Rise Building using Tuned Viscous Mass Dampers installed across Three Consecutive Storeys, in: Proceedings of the Twelfth International Conference on Computational Structures Technology, Naples, Italy, 2014: p. 225. https://doi.org/10.4203/ccp.106.225.